



# UBAP2L-driven stress granule formation links oxaliplatin resistance to gastric cancer



Chaorui Wu<sup>1,2,11</sup>, Yu Yan<sup>3,11</sup>, Qichen Chen<sup>4,11</sup>, Zhiying Lian<sup>1</sup>  , Jiayong He<sup>1</sup>, Ruoyu Ling<sup>5</sup>, Xuetao Lei<sup>6</sup>, Yanmei Peng<sup>7,8</sup>, Boyang Zheng<sup>1</sup>, Qingbin Yang<sup>1</sup>, Gengtai Ye<sup>1</sup>, Wenhui Ma<sup>9</sup> & Guoxin Li<sup>1,10</sup>  

Stress granules (SGs), which are phase-separating organelles that serve as protective cellular mechanisms in response to various harmful stimuli, have an unclear role in oxaliplatin resistance. Here, we establish a causal link between SG formation and oxaliplatin resistance in GC. Notably, we identify a key SG nucleator, namely, ubiquitin-associated protein 2-like (UBAP2L), as a previously unrecognized critical factor in mediating oxaliplatin resistance. UBAP2L-nucleated SG-mediated inhibition of apoptosis is associated with the recruitment of receptor of activated protein C kinase 1 (RACK1), a known promoter of apoptosis, to these entities. Transcriptional upregulation of UBAP2L is enhanced by oxaliplatin-induced phosphorylation and activation of heat shock factor protein 1 (HSF1) via AKT. Inhibiting either SG or HSF1 significantly overcomes oxaliplatin resistance *in vivo*. These findings demonstrate that UBAP2L-nucleated SGs play a vital role in mediating oxaliplatin resistance, with elevated SG levels emerging as a promising therapeutic target for overcoming this resistance.

Despite advancements in treatment, the prognosis for patients with advanced gastric cancer (GC) remains bleak due to chemotherapy resistance. Oxaliplatin is primarily used for the first-line chemotherapy for GC. The emergence of oxaliplatin resistance undermines treatment efficacy and increases recurrence rates, highlighting the need to investigate the underlying molecular mechanisms to improve patient outcomes.

Recent evidence suggests that oxaliplatin leads to a distinct translational arrest mechanism compared to cisplatin and carboplatin<sup>1</sup>. Oxaliplatin results in the disruption of the normal protein synthesis machinery, causing a slowdown or complete halt in translation. This translational arrest is a key trigger for the formation of stress granules (SGs), which are cytoplasmic aggregates that form when translationally stalled mRNAs and their associated proteins accumulate. SGs, composed of proteins and RNA, serve as important sites for the regulation and storage of mRNAs, facilitating rapid adaptive responses to stress<sup>2,3</sup>. By modulating translation and sequestering pro-apoptotic factors, SGs promote cell survival under stressful conditions<sup>4,5</sup>. However, the direct evidence linking SGs formation to cancer cell adaptation under oxaliplatin stress is still lacking.

The formation of SGs has been well-characterized in terms of liquid-liquid phase separation (LLPS), a process driven by the interactions within a core protein-RNA network<sup>6</sup>. LLPS is a fundamental biophysical process in which biomolecules, such as proteins and nucleic acids, spontaneously separate into dense liquid-like condensates within cells due to weak, multivalent interactions<sup>7,8</sup>. This network comprises 36 proteins and their

associated mRNAs, which undergo LLPS when their interactions exceed a critical threshold<sup>9</sup>. These interactions are unevenly distributed within the network, indicating that specific proteins play more pivotal roles in SG formation. It has also been proposed that the key nucleators of SG formation may vary depending on the type of stress. However, the specific proteins responsible for SG formation in response to oxaliplatin treatment remain unidentified.

In this study, we aim to elucidate the role of SGs in oxaliplatin resistance and identify the core SG proteins involved in this process. By advancing our understanding of the mechanisms behind SG formation and their role in oxaliplatin resistance, we hope to identify novel therapeutic targets that could improve treatment outcomes for GC patients facing oxaliplatin resistance.

## Materials and Methods

### Human samples

Human tissue samples were collected from 78 histologically confirmed GC patients (22 received preoperative CapeOX [capecitabine and oxaliplatin] or FOLFOX [5-fluorouracil, leucovorin calcium, and oxaliplatin] chemotherapy), associated clinicopathological information, as well as fresh human GC and adjacent normal tissues, were obtained from the Department of General Surgery at Nanfang Hospital, Southern Medical University and OUTDO BIOTECH (Shanghai). The condition of all samples was confirmed pathologically. Approval for the collection of human samples and all

experiments were approved by the Institutional Review Board (IRB) of Nanfang Hospital, Southern Medical University. Written informed consent was obtained from all participants prior to their inclusion in the study. All ethical regulations relevant to human research participants were followed.

### Cell lines and culture

AGS, HGC-27, MKN-45, and SNU-216 were obtained from American Type Culture Collection (ATCC). SGC-7901, MGC80-3, and BGC-823 were obtained from the Cell Bank, Shanghai Institute of Biochemistry and Cell Biology (SIBCB). All cell lines were validated by STR DNA profiling and tested negative for mycoplasma by PCR. The tumor-derived oxaliplatin-resistant cell line (TDOXR) was isolated from xenograft tumors in nude mice that were treated with multiple cycles of oxaliplatin, resulting in the acquisition of resistance. All cell lines were cultured in Dulbecco's Modified Eagle's Medium (DMEM), supplemented with 10% fetal bovine serum (FBS), in a humidified incubator at 37 °C with a 5% CO<sub>2</sub> atmosphere.

### Mouse models

Eight-week-old female nude mice were purchased from BesTest Biotechnology in Zhuhai, Guangdong. Three-month-old female spontaneous GC mice were generously provided by Prof. Shun Li (Shenzhen Majory Biotechnology Co., Ltd.). All animal experiments were approved by the Animal Care and Use Committee of Shenzhen Majory Biotechnology Co., Ltd. All animals were placed under a 12-h light–dark cycle. Room temperature was maintained at 21 ± 1 °C with 55–70% humidity. All mice were bred and maintained under specific-pathogen-free conditions in individually ventilated cages, and we have complied with all relevant ethical regulations for animal use. Humane endpoints were strictly followed, and euthanasia was performed using cervical dislocation, which is consistent with the AVMA Guidelines for the Euthanasia of Animals.

GC cell lines (2 × 10<sup>6</sup> per armpit; including parental, TDOXR, MGC80-3-UBAP2L and control cells) were resuspended in a 1:1 mixture of PBS and Matrigel, totaling 150 µL, and implanted subcutaneously into the right armpit of 8-week-old female nude mice (5 mice per group). The xenografts were allowed to grow for one week before drug administration. Mice received oxaliplatin (5 mg/kg, three times weekly, intraperitoneally) in a vehicle of 10% glucose solution, ISRIB (4 mg/kg, once daily for two weeks, intraperitoneally) or DTHIB (5 mg/kg, once daily for two weeks, intraperitoneally) in a vehicle of 10% DMSO and 90% corn oil. Control mice underwent the same procedures but received only vehicle treatment. Electronic calipers is used to measure length (l) and width (w) of xenografts, and the formula (w<sup>2</sup> × l)/2 to determine tumor volume. The end point was defined as the time at which a progressively growing tumor reached 20 mm in its longest dimension or 2000 mm<sup>3</sup> in its tumor volume as approved by the Animal Care and Use Committee of Shenzhen Majory Biotechnology Co., Ltd.; in no experiments was this limit exceeded.

For the establishment of oxaliplatin-resistant human GC xenografts, MGC80-3 cells (parental cells) were transplanted subcutaneously into nude mice. When tumor volumes reached 50–100 mm<sup>3</sup>, mice were intraperitoneally injected oxaliplatin (5 mg/kg/day, intraperitoneally) on days 1, 3, and 5 of each cycle, in according to previous researches<sup>10,11</sup>. Each cycle was one week in duration. Mice typically underwent two or more cycles of oxaliplatin treatment. Drug-free periods were included between cycles to allow for recovery. Once the mice exhibited signs of weakness due to chemotherapy-related side effects, the tumors were excised, digested with Collagenase IV, and cultured ex vivo. These cells were then retransplanted into nude mice, and oxaliplatin treatment was resumed once tumors regrew to 50–100 mm<sup>3</sup>, continuing until oxaliplatin resistance was acquired (indicated by no further shrinkage upon treatment).

To fully capture the complexity of tumor environment, we utilized a spontaneous GC mice model (crossing the gastric epithelium-specific Cre strain *Claudin18cre<sup>Ert2</sup>* with mice carrying conditional alleles for *Kras<sup>LSL-G12D/+</sup>*, *Trp53<sup>loxP/loxP</sup>*, and *Apc<sup>loxP/loxP</sup>*). The mice were all crossed onto the C57Black6/J background. Tumorigenesis was initiated at 8 weeks of age by intraperitoneal injection of 2.5 mg tamoxifen dissolved in 100 µl corn oil

to induce Cre recombination. Starting at 12 weeks of age, mice received intraperitoneal oxaliplatin treatment (5 mg/kg, three times per week, for 4 weeks). Following oxaliplatin treatment, the animals were euthanized, and their tissues were collected for histological and immunofluorescence analysis.

### Cell transfection

All plasmids were constructed by GENEYUAN Co., Ltd. (Guangzhou, China). The coding region of UBAP2L was cloned into the GEYB417 vector in-frame with a His tag, which conferred resistance to UBAP2L shRNA#1, using mutagenesis. This wild-type plasmid was retained as the starting material for generating His-tagged UBAP2L deletion mutants, including UBAP2L with amino acids 1–290 deleted. GC cells were stably transfected with lentiviruses targeting human UBAP2L-knockdown (KD), UBAP2L-overexpression, or a negative control (NC) from GeneChem (Shanghai, China). Following a 24-h incubation with the Lentivirus Enhancement Reagent Envirus, the medium was replaced. After an additional 48 h, successfully transfected cells (GFP +) were selected using 5–10 mg/mL puromycin for three to five days and isolated through single-cell colony formation. For cell viability assay, GC cells were transiently transfected with small interfering RNAs targeting human *G3BP1*, *UBAP2L*, *UBAP2*, *TIA1*, *PRRC2C*, or NC (from Tsingke Bio, Beijing, China) using lipofectamine 3000, according to the manufacturer's instructions. Transfection efficiency was confirmed by qRT-PCR and western blotting after cell collection. The siRNA sequences used are listed in Supplementary Table 4.

### Tumor-derived cancer cell isolation

GC xenograft tumors were separated from mice and placed in sterile conical tubes containing DMEM supplemented with 10% FBS and 1% penicillin-streptomycin on ice immediately. The digestion mixture was transferred to 15-mL centrifuge tubes with DMEM supplemented with 10 mg/mL DNase I, and 0.5 mg/mL Collagenase IV. The tubes were put on a rotator and incubated at 37 °C for 1 h. After that, cells were centrifuged at 1000 rpm for 3 min, and the cell pellets were resuspended in DMEM supplemented with 10% FBS and 1% penicillin-streptomycin-amphotericin B before being plated into a cell culture flask.

### Tissue immunohistochemistry (IHC) and Immunofluorescence (IF)

For IHC, tissue samples were first rinsed in PBS and then fixed in 10% formalin for 24 h. They were placed in cassettes and stored at 4 °C in 70% ethanol until paraffin embedding. The samples were sectioned at 5 µm and mounted on glass slides. To prepare the tissue sections, they were deparaffinized using xylene and rehydrated with a reversed ethanol gradient. Heat-mediated antigen retrieval was performed with a citrate buffer (0.01 M sodium citrate/0.05% Tween-20, pH 6.0). The sections were then blocked for 1 h at room temperature (RT) in a solution containing 10 mmol/L Tris-HCl, 0.1 M MgCl<sub>2</sub>, 0.05% Tween-20, 1% BSA, and 10% FBS. Overnight incubation at 4 °C with primary antibodies was carried out in a humidified chamber. After washing the slides in TBST (0.1% Tween-20 in TBS), the appropriate secondary antibodies were applied for 1 h at RT. Following another wash in TBST, the target proteins were visualized using a DAB Chromogen Kit, resulting in a brown stain that indicated the presence of the targeted molecules. The slides were then counterstained with diluted hematoxylin for 3 to 5 min, and representative images were captured using an Olympus CX23 Digital Microscope.

For IF, tumor tissues were embedded in O.C.T. medium and sectioned at a thickness of 12 µm. The sections were fixed and subsequently stained with antibodies. Cells cultured on coverslips were fixed in 4% paraformaldehyde, immunostained, and then mounted onto glass slides. Tissue samples were blocked for 1 h at RT using a solution of 10 mmol/L Tris-HCl, 0.1 M MgCl<sub>2</sub>, 0.05% Tween-20, 1% BSA, and 10% FBS. The slides were then incubated with primary antibodies for 1 h at RT in a humidified chamber. After washing in TBST, sections were treated with appropriate fluorescence-conjugated secondary antibodies for 1 h at RT. Following another TBST wash, the sections were stained with DAPI for 5 min at room temperature.

Finally, the slides were scanned using a PANNORAMIC Digital Slide Scanner (3DHISTECH Ltd.). Antibodies used in this study are listed in Supplementary Table 5.

### Terminal deoxynucleotidyl transferase dUTP nick-end labeling (TUNEL) assay

Apoptotic cells were detected using the TUNEL assay, following the manufacturer's protocol. Briefly, cultured cells or tissue sections were fixed in 4% paraformaldehyde for 15 minutes at room temperature. After fixation, samples were permeabilized using 0.1% Triton X-100 for 10 minutes, followed by washing with phosphate-buffered saline (PBS). The TUNEL reaction mixture was prepared by incubating the samples with terminal deoxynucleotidyl transferase (TdT) enzyme and fluorescein-labeled dUTP for 60 minutes at 37 °C in a humidified chamber. After the reaction, excess labeling reagent was removed by washing with PBS. Nuclei were counterstained with 4',6-diamidino-2-phenylindole (DAPI) to visualize total cell populations. Positive control samples were treated with DNase I to induce DNA fragmentation, while negative control samples lacked the TdT enzyme. The slides were scanned using a PANNORAMIC Digital Slide Scanner and the TUNEL-positive area was quantified.

### Imaging quantification

Western blot images were analyzed using ImageJ software. For each lane, the region of interest (ROI) was manually defined around the protein band of interest and the loading control. Background-subtracted integrated density was measured for each band. The intensity of the target protein was normalized to the corresponding loading control (e.g.,  $\beta$ -actin) to account for loading variations. Normalized intensity values were calculated as the ratio of target protein intensity to loading control intensity. At least three independent biological replicates were analyzed. Unedited raw images and quantified data are provided in the Supplementary Materials for transparency.

All IHC slides were independently evaluated by two experienced pathologists who were blinded to the clinical data. Discrepancies in scoring were resolved through consensus discussion. Staining intensity was scored on a scale of 0 to 3 (0 = no staining, 1 = weak staining, 2 = moderate staining, 3 = strong staining). The percentage of positively stained cells was also recorded (0 = 0%, 1 = 1–25%, 2 = 26–50%, 3 = 51–75%, 4 = 76–100%). The final IHC score was calculated by multiplying the staining intensity score by the percentage score, resulting in a range of 0 to 12. For quantifying the tumor area positive for CC3 or TUNEL, maximum projection images were thresholded to create black-and-white images, enabling the identification of both the tumor area positive for the protein and the total tumor area per field. Batch processing was applied to ensure consistent thresholding across all images from each experiment. The relative CC3-positive and TUNEL-positive area per tumor was calculated as a fraction of the total tumor area for each field and averaged across all fields.

Images were randomly captured from five different fields, each containing at least 50 cells. Background intensity was subtracted from all images. The "Analyze Particles" plugin was used to assess the total SG area in relation to the total cell area. The total cell area for each image was outlined and measured using ImageJ's selection and measurement tools. The SG index was calculated by comparing the total SG area to the total cell area for each field, with results averaged across all fields. To determine the percentage of cells positive for SGs, a manual count was performed on a minimum of 200 cells per experimental condition across at least five random fields from three independent experiments.

### Chromatin immunoprecipitation (ChIP) assay and Co-immunoprecipitation (CoIP)

ChIP was carried out using the SimpleChIP Enzymatic Chromatin IP Kit (Magnetic Beads) in accordance with the manufacturer's guidelines. Cells were crosslinked with 1% formaldehyde for 10 min, followed by the addition of glycine for 5 min to stop the crosslinking. After washing with cold PBS, the cells were collected and treated with micrococcal nuclease for 20 min at

37 °C. The nuclear membranes were then lysed using three sets of 20-second ultrasonic pulses. From each sonicated sample, 50  $\mu$ l was reserved to assess DNA concentration and fragment size. The cell lysates were incubated overnight at 4 °C with either 2  $\mu$ g of normal rabbit IgG as a negative control, 2  $\mu$ g of ChIP-grade anti-HSF1 antibody (Cell Signaling Technology), or 10  $\mu$ l of anti-Histone H3 (D2B12) XP rabbit monoclonal antibody. Following incubation, 30  $\mu$ l of Protein G magnetic beads was added to each immunoprecipitation (IP) reaction, and the mixtures were rotated for 2 h at 4 °C. The beads were subsequently collected, washed, and treated with proteinase K for 2 h at 65 °C. DNA was then purified using spin columns, amplified by PCR, and analyzed via electrophoresis. Primer sequences and antibodies used in this study are detailed in Supplementary Table 4 and Supplementary Table 5, respectively. For CoIP, briefly, protein was isolated using RIPA buffer (50 mM Tris, 150 mM NaCl, 1 mM EDTA, 1% NP-40, 1% sodium deoxycholate, 1% SDS) for immunoblotting or with IP lysis buffer (20 mM Tris, 150 mM NaCl, 1 mM EDTA, 1 mM EGTA, 1 mM sodium pyrophosphate, 1 mM  $\beta$ -glycerophosphate, 1% Triton X-100) for lysate to be used for IP. Lysates were subjected to SDS/PAGE and subjected immunoblotting with indicated antibodies.

### Luciferase reporter assay

To assess *UBAP2L* promoter activity, cells were seeded in 24-well plates and transfected with the luciferase reporter plasmids using Lipofectamine 3000 (Invitrogen) according to the manufacturer's instructions. The wild-type and three mutant reporter constructs each contained the firefly luciferase gene driven by the *UBAP2L* promoter region, and a Renilla luciferase plasmid (as a transfection control) was co-transfected into each well. After 24 to 48 hours post-transfection, cells were harvested using Passive Lysis Buffer, and luciferase activity was measured using the Dual-Luciferase Reporter Assay System according to the manufacturer's protocol. The luminescence of firefly and Renilla luciferase was quantified using a luminometer (e.g., TD-20/20 Luminometer, Turner Designs). Firefly luciferase activity was normalized to Renilla luciferase activity to control for transfection efficiency. Data were expressed as relative luciferase units (RLU) and are presented as the mean  $\pm$  standard deviation (SD) from at least three independent experiments.

### Western blotting

For protein extraction, cells were lysed for 30 min on ice using radio-immunoprecipitation assay (RIPA) buffer supplemented with a protease and phosphatase inhibitor cocktail. The lysate was then centrifuged at 12,000 g for 15 min at 4 °C, and the supernatant containing soluble proteins was collected. Protein concentration was determined using the bicinchoninic acid (BCA) reagent. The lysates were heated at 100 °C in NuPAGE LDS sample buffer (4x) for 3–5 min, then separated by sodium dodecyl sulfate polyacrylamide gel electrophoresis (SDS-PAGE) and transferred electrophoretically to a polyvinylidene fluoride (PVDF) membrane (Millipore, MA, USA). The membranes were blocked with 10% BSA and incubated overnight at 4 °C with primary antibodies. After washing with TBST, the membranes were incubated for 2 h at 4 °C with species-specific HRP-conjugated secondary antibodies. Signals from the immunoreactive proteins were detected using a chemiluminescence ECL Detection Kit, and the corresponding bands were visualized with the ChemiDoc Imaging System (BioRad, California, USA). Antibodies used in this study are listed in Supplementary Table 4.

### Purification of stress granules and mass spectrometry analysis

Briefly, oxaliplatin-treated MGC-803 cells were harvested, washed with cold PBS, and resuspended in 1 mL of Nuclei Isolation Buffer (NIB: 0.5% NP40; 50 mM NaCl; 5 mM MgCl<sub>2</sub>; 50 mM Tris-HCl, pH 7.6; 5 mM  $\beta$ -mercaptoethanol), supplemented with 1X complete protease inhibitor. The samples were gently suspended by passing them through a 25-gauge 5/8 mm needle attached to a 1 mL syringe 8 times and then incubated on ice for 5 minutes. The cells were spun at 1800 g for 2 minutes at 4 °C, and the supernatant was further spun at 18,000 g for 20 minutes at 4 °C to pellet the SGs. After discarding the supernatant, the pellets were washed with 1 mL of

NIB, followed by another centrifugation at 18,000 *g* for 20 minutes at 4 °C. The soluble supernatant was discarded, and the SG-enriched pellet was resuspended in 900  $\mu$ L of NIB. To isolate the SGs, the 900  $\mu$ L resuspended material was split into 2 tubes, with 4  $\mu$ g of rabbit IgG (isotype control) or rabbit anti-UBAP2L added to each tube for overnight incubation at 4 °C with rotation. Next, 50  $\mu$ L of protein-G coated Dynabeads, pre-washed with NIB, were added and incubated for 1 hour with rotation at room temperature. The beads and immunoprecipitates were captured using a magnet and washed 3 times for 5 minutes. All buffers contained 1X complete protease inhibitor (EDTA-free). The beads were then denatured in Laemmli buffer with NuPAGE sample reducing agent at 95 °C for 5 minutes. Finally, the beads were removed, and the samples were sent to mass spectrometry analysis. Samples were subjected to trypsin digestion, HPLC-MS/MS, and data analysis by AimsMass Biotechnology Co., Ltd (Guangzhou, China).

### High-performance liquid chromatography–mass spectrometry (HPLC-MS)

The fraction was resuspended in loading buffer (0.1% FA, 2% ACN) and separated with an Ultimate 3000 nano-LC system equipped with a C18 reverse phase column (100- $\mu$ m inner diameter, 10-cm long, 3- $\mu$ m resin from MichromBioresources, Auburn, CA). Separate the peptides with the following parameters: (1) mobile phase A: 0.1% FA, 5% ACN, dissolved in water; (2) mobile phase B: 0.1% FA, 95% ACN; (3) flow rate: 300 nL/min; (4) gradient: B-phase increased from 5% to 40%, 70 min. Then, the LC eluent was subject to Q Exactive (Thermo Fisher) in an information dependent acquisition mode. MS spectra were acquired across the mass range of 400–1,250 *m/z* in high resolution mode (>30,000) using 250 ms accumulation time per spectrum. A maximum of 20 precursors per cycle were chosen for fragmentation from each MS spectrum with 100 ms minimum accumulation time for each precursor and dynamic exclusion for 20 s. Tandem mass spectra were recorded in high sensitivity mode (resolution > 15,000) with rolling collision energy on. Raw data were searched against the Uniprot human protein database using the SEQUEST algorithm embedded in the Protein Discoverer 1.3 Software (Thermo Fisher Scientific, Waltham, MA, USA). The following parameters were applied during the database search: 10 ppm precursor mass error tolerance, 1 Da fragment mass error tolerance, static modifications of carbamidomethylation for all cysteine residues, flexible modification of oxidation modifications for methionine residues, and one missed cleavage site of trypsin was allowed. FDR < 0.01 was used as filtering criteria for all identified peptides. Only proteins identified with two or more unique peptides were considered, and proteins identified with the same set of peptides were grouped.

### Puromycin incorporation assay for assessing protein synthesis

Cells were incubated with 10  $\mu$ g/mL puromycin for 30 minutes to label newly synthesized proteins. After incubation, cells were washed with ice-cold PBS to remove excess puromycin and lysed in RIPA buffer. The incorporation of puromycin into nascent proteins was detected by specific anti-puromycin antibody binding to puromycin-labeled peptides. The intensity of puromycin incorporation was quantified by standard detection methods.

### Quantitative real-time PCR (qRT-PCR)

Total RNA was extracted from the cell lines using the RNA-Quick Purification Kit following the manufacturer's instructions. RNA concentration was measured using a NanoDrop 1000 (Thermo Fisher Scientific, USA), and complementary DNA was synthesized from 2  $\mu$ g of RNA using the PrimeScript RT Reagent Kit. qRT-PCR was conducted with TB-Green dye on a Corbett Rotor-Gene 3000 thermocycler, adhering to the manufacturer's protocol. The amplification conditions were as follows: 95 °C for 30 sec, followed by 40 cycles of 95 °C for 5 sec, 60 °C for 34 sec, and ending with 95 °C for 15 sec. All experiments were performed in triplicate. Analysis of the cycle threshold (Ct) values indicated differences in mRNA expression levels among the groups, with relative expression levels of each target gene normalized to the corresponding  $\beta$ -actin mRNA levels. Primer sequences are detailed in Supplementary Table 4.

### Cell assays

For cell proliferation assays, cells were seeded in triplicate at a density of 2000 cells per well in 96-well plates. For cell viability assays, a density of 5000 cells per well was seeded and cultured for 18–24 h. GC cells were treated with compounds at specified concentrations for indicated time periods. Cell proliferation and viability was assessed using the CCK-8 assay at predetermined intervals. Specifically, 10  $\mu$ L of CCK-8 solution was added to each well, and the cells were incubated at 37 °C for 2 h. The absorbance at 450 nm (OD450) was then measured using a microplate reader. Relative viability was calculated by normalizing the results to those obtained from the corresponding DMSO-treated control, unless otherwise specified. Three independent experiments were conducted.

For the colony formation assay,  $5 \times 10^5$  GC cells were seeded evenly in cell culture plates, with three wells per group, and cultured for 18–24 h. The cells were treated with oxaliplatin at the specified concentrations for 24 h. After treatment, the cells were washed, fixed with methanol for 20 min, and stained with 0.5% crystal violet. Key reagents or sources of all experimental assays in this study are detailed in Supplementary Table 6.

### Flow cytometry

Apoptotic cells were stained using Annexin V and propidium iodide (PI) according to the manufacturer's protocol (Yeaston). Flow cytometry was conducted using a CytoFLEX-S flow cytometer (Beckman Coulter), and the data were analyzed with FlowJo software.

### Analysis of public database

Microarray data were downloaded from the GEO and analyzed with Seurat (v4.2.0) in R (v 4.1.2) using Rstudio. Analysis of TCGA datasets was performed with cBioportal and GEPIA<sup>12,13</sup>. Survival data are analyzed through the Kaplan-Meier Plotter database<sup>14</sup>.

### Quantification and statistical analysis

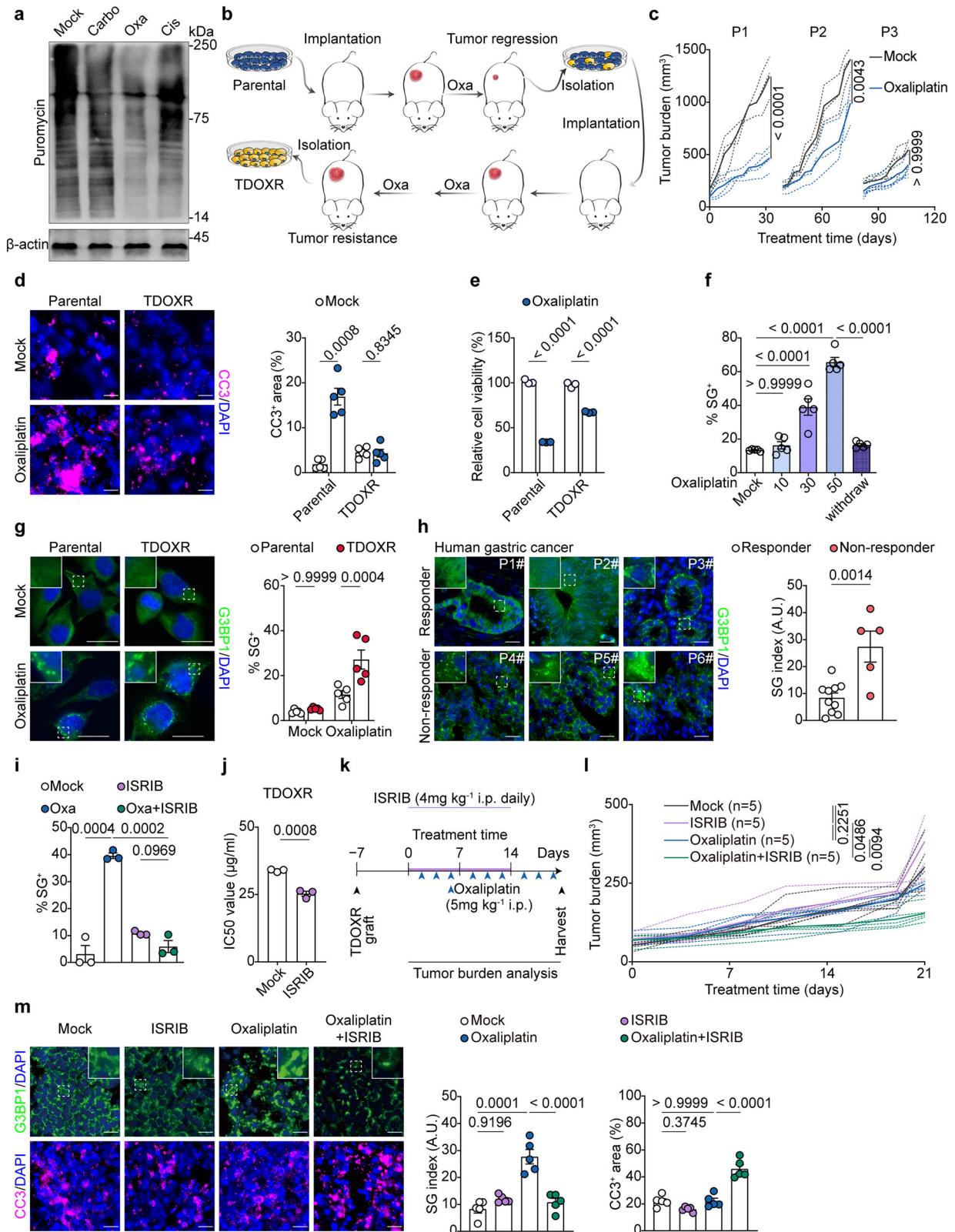
For details on sample size (*n*) and statistical analysis, please refer to the figure legends or experimental methods. All values of *n* represent individual mice or individual samples. Sample sizes were determined based on prior experience with similar experiments. Cell culture assays were conducted in three independent experiments. Quantitative data are presented as the mean  $\pm$  SEM. Kaplan-Meier curves were generated with 95% confidence intervals (CI), and log-rank tests were used to compare survival between groups. Hazard ratios (HR) and 95% CI were calculated using Cox proportional hazards models. IC50 values were determined using nonlinear regression. The paired sample *t*-test or two independent sample *t*-test was used for comparisons between two groups. Comparisons between groups were performed using one-way or two-way ANOVA, followed by Bonferroni's post hoc test for multiple comparisons, unless otherwise specified. Gene expression data from TCGA datasets were analyzed using Mann-Whitney U test or Student's *t*-test for two groups, and one-way ANOVA with Bonferroni's post hoc test for multiple groups. Correlations between HSF1 expression and UBAP2L expression were calculated using Spearman's rho correlation coefficients. Data were analyzed using Prism 9.0 (GraphPad Software Inc.). Statistical significance was set at *P* < 0.05.

### Statistics and reproducibility

All statistical methods used in this study are described in the relevant sections. For western blot and cell culture assay results, the data were reproduced in three independent experiments (or more, as specified), and representative data are shown. Sample sizes were not predetermined using statistical methods. Statistical analyses were performed using GraphPad Prism 9.0 software or Microsoft Excel 2023.

### Reporting summary

Further information on research design is available in the Nature Portfolio Reporting Summary linked to this article.



**Results**

**Enhanced SG formation contributes to oxaliplatin resistance**

Recent evidence suggests that oxaliplatin leads to a translational arrest mechanism distinct from that of cisplatin and carboplatin<sup>1</sup>. In line with this finding, we demonstrate that only oxaliplatin triggers significant translational arrest, as evidenced by a notable reduction in de novo protein

synthesis, measured by puromycin incorporation assay (Fig. 1a). A key mechanism underlying stress-induced translational arrest is the phosphorylation of eukaryotic initiation factor 2 $\alpha$  (eIF2 $\alpha$ ) at serine 51, which disrupts the translational initiation complex<sup>15</sup>. Our observations confirm this mechanism, as we detected increased phosphorylation of eIF2 $\alpha$  at serine 51 following oxaliplatin treatment (Supplementary Fig. 1a). This therapeutic

**Fig. 1 | Enhanced SG formation contributes to oxaliplatin resistance.** **a** Western blot (WB) analysis of whole cell extracts (WCEs) from MGC80-3 cells treated with carboplatin (carbo), oxaliplatin (oxa), or cisplatin (cis). **b** Schematic representation of the establishment of oxaliplatin-resistant xenograft models using MGC80-3 (parental) cell line. **c** Tumor burden kinetics of xenograft model (parental) in nude mice treated with oxaliplatin treatment (5 mg kg<sup>-1</sup>, three times per week) across different passages. “Px” denotes Passage x. **d** Representative immunofluorescence (IF) staining of the cell death marker cleaved caspase-3 (CC3) (left) and its quantification (right) in parental and tumor-derived oxaliplatin-resistant (TDOXR) tumors on nude mice treated with either oxaliplatin or vehicle control (n = 5 mice per group). **e** Relative cell viability of parental and TDOXR cell following oxaliplatin treatment (10 µg/ml, 24 h). **f** Quantification of the stress granule (SG) marker G3BP1-positive parental cells treated with oxaliplatin at increasing concentrations (0, 10, 30, 50 µg/ml for 5 h) or following drug withdrawal (50 µg/ml followed by a 3 h withdrawal) (n = 5 fields per group). **g** Representative IF staining of G3BP1 (left) and quantification (right) of G3BP1<sup>+</sup>SG-positive parental and TDOXR cells treated with oxaliplatin (10 µg/ml) for 8 h or vehicle control (n = 5 fields per group). **h** Representative IF staining of G3BP1 (left) and quantification (right) of the SG index of

tumor biopsies from responsive (n = 10) and non-responsive (n = 5) gastric cancer (GC) patients treated with preoperative oxaliplatin-based chemotherapy. **i** Quantification of G3BP1<sup>+</sup>SG-positive parental cells treated with vehicle control, oxaliplatin (10 µg/ml, 5 h), ISRIB (5 µM, 5 h), or both treatments. **j** Half-maximal inhibitory concentration (IC<sub>50</sub>) assay for oxaliplatin in TDOXR cells treated with either vehicle control or ISRIB (5 µM) for 24 h. **k** Schematic of the experimental design for the TDOXR mouse model. **l** Quantification of tumor burden in TDOXR xenografts in nude mice treated with oxaliplatin (5 mg kg<sup>-1</sup>, three times per week, n = 5 mice per group), ISRIB (4 mg kg<sup>-1</sup>, once daily for two consecutive weeks), both, or vehicle control. **m** Representative IF staining (left) of G3BP1 and CC3, as well as the quantification (right) of SG index and CC3-positive area from xenograft tumors shown in **l**. Dashed line areas are shown with magnification. Scale bars, 20 µm. P values determined by one-way analysis of variance (ANOVA) with Bonferroni's post hoc test (**f**, **i**, **m**), two-way ANOVA with Bonferroni's post hoc test (**c**, **l**) or two-tailed unpaired *t*-test (**d**, **e**, **g**, **h**, **j**). Data are represented as the mean ± s.e.m. (**d**–**j**, **m**). Data are pooled biological replicates (**c**, **d**, **h**, **l**, **m**) or representative of three independent experiments (**a**, **e**, **f**, **g**, **i**, **j**).

distinction underscores the focus of our investigation on oxaliplatin resistance.

Mimicking oxaliplatin resistance through drug exposure in cell culture may not accurately reflect the long-term exposure experienced by patients, leading to the development of resistance mechanisms that differ from those observed in clinical settings<sup>16</sup>. To recapitulate oxaliplatin resistance in vivo, we initially tested the oxaliplatin sensitivity of multiple GC cell lines and identified MGC80-3 as the most sensitive line (Supplementary Fig. 1b). We then implanted MGC80-3 cells (parental cells) subcutaneously into nude mice, subjecting them to multiple cycles of oxaliplatin until resistance developed, finally establishing an oxaliplatin-resistant GC xenograft model (Fig. 1b, c). Consistently, these resistant tumors exhibited lower levels of cleaved caspase-3 (CC3)-positive and TUNEL-positive area, both apoptosis markers, thereby confirming establishment of acquired resistance in vivo (Fig. 1d and Supplementary Fig. 1c). To facilitate the investigation of the underlying resistant mechanism, we derived tumor-derived oxaliplatin-resistant cells (TDOXR) from the resistant xenograft tumors. The TDOXR cells demonstrated significant resistance to oxaliplatin ex vivo (Fig. 1e).

Previous studies indicate that oxaliplatin may induce the formation of SGs<sup>17</sup>. However, the direct evidence establishing a link between SGs and cellular adaptation to oxaliplatin-induced stress is currently lacking. To address this question, we initially visualize the SG in GC cells by immunofluorescence (IF) staining of G3BP1, a well-known SG marker<sup>18,19</sup>. Consistent with oxaliplatin's unique ability to induce translational arrest, only oxaliplatin triggered the formation of SGs, unlike carboplatin and cisplatin (Supplementary Fig. 1d). Furthermore, reflecting the dynamic nature of SG assembly and disassembly in response to stress, SG levels in GC cells increased approximately fourfold after oxaliplatin exposure, followed by disaggregation upon drug withdrawal (Fig. 1f and Supplementary Fig. 1e). Oxaliplatin treatment resulted in a higher prevalence of G3BP1<sup>+</sup>SG-positive cells in TDOXR compared to parental cells (Fig. 1g). Furthermore, the G3BP1<sup>+</sup>SGs formation was stronger in unresponsive human GC samples compared with responsive GC samples (Fig. 1h). These findings indicate that oxaliplatin promotes SG formation, suggesting a close relationship between SGs and oxaliplatin resistance.

To evaluate the dependence of oxaliplatin resistance on SG, we utilized ISRIB, a small-molecule inhibitor that effectively inhibits SG assembly<sup>20</sup>. ISRIB remarkably reduced the formation of G3BP1<sup>+</sup>SG induced by oxaliplatin (Fig. 1i, and Supplementary Fig. 1f). Consistently, ISRIB restored oxaliplatin sensitivity of TDOXR cells ex vivo (Fig. 1j). We then treated nude mice bearing TDOXR xenograft tumors with ISRIB, oxaliplatin, a combination of both, or vehicle control (Fig. 1k). Despite their strong resistance to oxaliplatin, TDOXR tumors exhibited improved sensitivity to the ISRIB-oxaliplatin combination (Fig. 1l and Supplementary Fig. 1g). No significant weight loss was observed in ISRIB-treated mice, indicating a favorable safety profile (Supplementary Fig. 1h). IF staining revealed a reduction in SGs

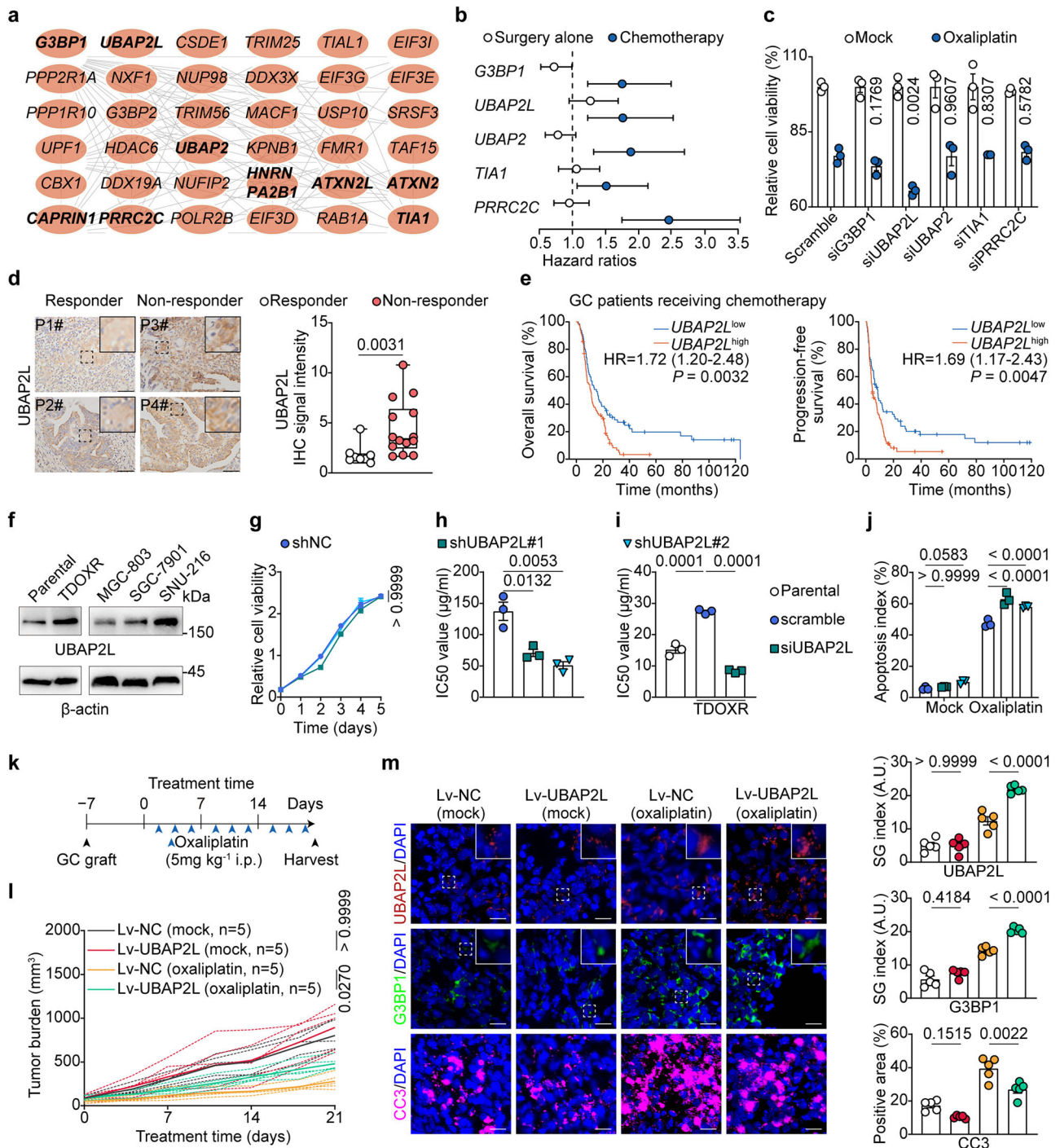
(labeled by G3BP1) and increase of CC3-positive or TUNEL-positive area in the combination treatment group (Fig. 1m and Supplementary Fig. 1i). Collectively, these in vitro and in vivo findings support the conclusion that increased SG formation significantly contributes to oxaliplatin resistance.

### UBAP2L is a key SG protein associated with oxaliplatin resistance

Recent studies demonstrated that SG formation is orchestrated by the interactions of approximately 36 core SG nucleator proteins along with their associated mRNAs<sup>9</sup>. To identify the principal SG nucleator protein responsible for oxaliplatin resistance, we analyzed the gene expression profiles of core SG nucleators in GC versus normal specimens through the Cancer Genome Atlas (TCGA), their association with chemoresistance by analyzing survival of GC patients and assessed their effects on oxaliplatin sensitivity in vitro (Supplementary Fig. 2a). The SG network consisting of 36 core nucleator proteins are illustrated (Fig. 2a). Among these, five SG nucleator genes—*G3BP1*, *UBAP2L*, *UBAP2*, *TIA1*, and *PRRC2C*—exhibited significant upregulation in GC and correlation with poor survival outcomes following chemotherapy (Fig. 2b and Supplementary Fig. 2b). Notably, silencing *UBAP2L* but not other genes led to a profound inhibition of oxaliplatin resistance in TDOXR cells (Fig. 2c). Additionally, we observed a consistent upregulation of *UBAP2L* expression in human GC samples compared to normal stomach tissues from our center (Supplementary Fig. 2c, d). The *UBAP2L* high-expression group is significantly associated with a higher proportion of CIN, EBV, or POLE subgroups (Supplementary Fig. 2e, Supplementary Table 1).

To validate the correlation between *UBAP2L* and oxaliplatin resistance, we assessed *UBAP2L* expression in primary tumor samples from GC patients who underwent oxaliplatin-based chemotherapy. Our findings indicate that the *UBAP2L* upregulation is associated with poor chemotherapy responses, with no significant correlations found between clinical response and common clinicopathological characteristics (Fig. 2d and Supplementary Table 2). Due to the absence of chemotherapy data in the TCGA (STAD) dataset, we turned to the KM-Plotter database to analyze the relationship between *UBAP2L* expression and chemotherapy response. Analysis revealed that *UBAP2L* levels negatively correlated with overall survival and progression-free survival in GC patients receiving chemotherapy, but not in those undergoing surgery alone (Fig. 2e and Supplementary Fig. 2f).

In our assessment, SGC-7901 and SNU-216 cells exhibited resistance to oxaliplatin, while MGC80-3 cells were the most sensitive among various GC cell lines (Supplementary Fig. 1a). Consistently, *UBAP2L* protein levels were higher in SNU-216 and SGC-7901 cells than in MGC80-3 cells. Notably, *UBAP2L* expression was also elevated in TDOXR cells compared to their parental counterparts (Fig. 2f). Thus, SNU-216 and SGC-7901 cells were engineered to stably express two independent small hairpin RNAs



(shRNAs) targeting *UBAP2L* or a negative control (NC) shRNA. MGC80-3 cells were modified to express either a *UBAP2L*-expressing recombinant lentivirus (Lv-*UBAP2L*) or a control vector (Lv-NC) (Supplementary Fig. 3a). Consistent with a role for *UBAP2L* in oxaliplatin stress adaptation, knockdown of *UBAP2L* had no impact on cell proliferation under normal growth conditions (Fig. 2g and Supplementary Fig. 3b), but impaired the intrinsic and acquired resistance of different GC cell lines to oxaliplatin (Fig. 2h, i and Supplementary Fig. 3c). Colony formation assays and flow cytometry analysis of apoptosis corroborated the above results (Fig. 2j, Supplementary Fig. 3d and Supplementary Fig. 4a, b). *UBAP2L* overexpression further confirmed the inductive effect of *UBAP2L* on oxaliplatin resistance (Supplementary Fig. 3b, c). On the other hand, knockdown of

*UBAP2L* impeded the migration and invasion abilities of common GC cell lines. In contrast, its overexpression enhanced the migration and invasion abilities (Supplementary Fig. 4c, d). Furthermore, we implanted oxaliplatin-sensitive GC cells (parental cells) with or without *UBAP2L* overexpression into nude mice and treated them with vehicle control or oxaliplatin (Fig. 2k). *UBAP2L* overexpression resulted in tumor progression compared to controls under oxaliplatin treatment, while vehicle-treated tumors showed no significant difference between groups (Fig. 2l and Supplementary Fig. 3e). Additionally, *UBAP2L* overexpression led to stronger formation of *UBAP2L*<sup>+</sup>SG and *G3BP1*<sup>+</sup>SG from sections of xenograft tumors, along with a significant decrease in CC3-positive or TUNEL-positive area under oxaliplatin treatment (Fig. 2m, and Supplementary Fig. 3f).

**Fig. 2 | UBAP2L is a key SG protein associated with oxaliplatin resistance.** **a** Core SG network comprising 36 genes<sup>9</sup>. Upregulated SG genes in tumor relative to normal tissue are indicated in bold (data from The Cancer Genome Atlas [TCGA]). **b** *G3BP1*, *UBAP2L*, *UBAP2*, *TIA1*, and *PRRC2C* expression negatively correlate with survival in GC patients receiving chemotherapy, but not in those undergoing surgery alone. **c** Relative cell viability of TDOXR cells with or without knockdown of the indicated SG genes following oxaliplatin treatment (10 µg/ml, 24 h). **d** Representative immunohistochemistry (IHC) staining of UBAP2L (left) and quantification (right) of IHC signal intensity in tumor biopsies from responsive ( $n = 8$ ) and non-responsive ( $n = 14$ ) GC patients treated with preoperative oxaliplatin-based chemotherapy. Scale bars, 50 µm. Boxes represent the 25th to 75th percentiles, whiskers denote minimum to maximum values, and the center line indicates the median. **e** Negative correlation of *UBAP2L* expression with overall survival and progression-free survival in GC patients receiving chemotherapy (data from the Kaplan-Meier Plotter database). **f** WB analysis demonstrating higher UBAP2L levels in three oxaliplatin-resistant cell lines (TDOXR, SGC-7901, SNU-216) compared to the oxaliplatin-sensitive cell line (MGC80-3). **g** Proliferation rates of SNU-216 cells expressing the indicated shRNAs. **h**, **i** UBAP2L knockdown inhibits

intrinsic and acquired oxaliplatin resistance. **h** IC50 assay for oxaliplatin in intrinsic oxaliplatin-resistant cells (SNU-216) expressing the indicated shRNAs. **i** IC50 assay for oxaliplatin in acquired oxaliplatin-resistant cells (TDOXR) with or without *UBAP2L* knockdown. **j** Quantification of AnnexinV<sup>+</sup>PI<sup>+</sup> SNU-216 cells with or without *UBAP2L* knockdown following treatment with oxaliplatin or vehicle control. **k** Experimental design to assess the effects of *UBAP2L* overexpression on oxaliplatin resistance in mouse model. **l** Tumor burden quantification for xenografts with or without *UBAP2L* overexpression in nude mice treated with oxaliplatin (5 mg/kg, three times per week,  $n = 5$  mice per group) or vehicle control. Lv-NC: negative control lentivirus; Lv-UBAP2L: lentivirus expressing UBAP2L. **m** Representative IF staining (left) of UBAP2L, G3BP1, and CC3, and quantification (right) of SG index and CC3-positive area from xenograft tumors of **l**. Scale bars, 20 µm. Dashed line areas are shown with magnification. *P* values determined by one-way ANOVA with Bonferroni's post hoc test (**h–j**), two-way ANOVA with Bonferroni's post hoc test (**g**, **l**), two-tailed unpaired *t*-test (**c**, **d**, **m**) or log-rank test (**b**, **e**). Data are represented as the mean ± s.e.m (**c**, **d**, **g–j**, **m**). Data are pooled biological replicates (**d**, **m**) or representative of three independent experiments (**c**, **f–j**).

### UBAP2L-mediated oxaliplatin resistance is SG-dependent

Oxaliplatin treatment effectively triggered the formation of UBAP2L<sup>+</sup>SGs, while drug withdrawal led to the disassembly of these granules (Supplementary Fig. 5a). Importantly, we observed a significantly higher proportion of UBAP2L<sup>+</sup>SG-positive cell in TDOXR cells after oxaliplatin treatment compared to parental cells (Fig. 3a). Oxaliplatin-resistant GC samples also exhibited increased UBAP2L<sup>+</sup>SG levels compared to sensitive samples (Fig. 3b). The ability of UBAP2L to regulate SG formation is governed by its ubiquitin-associated domain (UBA), Arg–Gly–Gly (RGG) motif and predicted RNA binding domains (RBD), which mediates the recruitment of SG components<sup>21</sup>. To establish a causal link between SG formation and oxaliplatin resistance, we utilized a UBAP2L mutant lacking the UBA, RGG and RBD domain (dN-UBAP2L). UBAP2L-knockdown GC cells were engineered to express shRNA-resistant UBAP2L wild-type (WT) or dN-UBAP2L (Fig. 3c). As anticipated, oxaliplatin-induced SG formation was rescued by the expression of shRNA-resistant WT-UBAP2L, but not dN-UBAP2L (Fig. 3d). Consistently, UBAP2L-WT expression rescued oxaliplatin resistance in UBAP2L-knockdown GC cells, whereas expression of dN-UBAP2L did not (Fig. 3e). Given the critical role of the UBA, RGG and RBD domain in SG formation, these results indicate that the rescue of oxaliplatin resistance by UBAP2L-WT is dependent on its SG-nucleating capacity. Given that cancer cells are exposed to various stressors and chemotherapeutic drugs, we further investigated whether UBAP2L knockdown influences SG formation under different stress conditions. Unlike carboplatin and cisplatin, fluorouracil (5-FU) was able to induce UBAP2L-positive SGs (Supplementary Fig. 5b), consistent with previous studies showing that the incorporation of 5-FU metabolites into RNA promotes SG assembly<sup>22</sup>. Similarly, UBAP2L knockdown sensitized GC cells to 5-FU, but not to carboplatin or cisplatin (Supplementary Fig. 5c). *UBAP2L* knockdown also diminished both UBAP2L<sup>+</sup>SG and G3BP1<sup>+</sup>SG formation in cells exposed to endoplasmic reticulum (ER) stress and heat shock (HS) (Fig. 3f, and Supplementary Fig. 5d, e), which indicate that UBAP2L is essential for SG assembly across multiple conditions, suggesting its potential involvement in the signaling pathways that regulate SG assembly. An early step in SG assembly is the translational arrest initiated by eIF2α phosphorylation at serine residue 51<sup>15</sup>. We revealed that eIF2α phosphorylation occurred similarly in cell lysates of different GC cell lines with *UBAP2L* expression modification (Fig. 3g and Supplementary Fig. 5f), indicating that UBAP2L is not required for eIF2α phosphorylation following stress.

G3BP1 is widely recognized as a central SG nucleator, raising questions about UBAP2L's independent or synergistic role in SG formation. Additionally, the recruitment of key signaling pathway components to SGs has previously been shown to influence apoptosis. To address these questions, we enriched SGs from oxaliplatin-treated GC cells using successive differential centrifugation, followed by affinity purification with anti-UBAP2L antibodies or IgG antibodies. The enriched samples were then subjected to

mass spectrometry analysis. Mass spectrometry analysis identified 216 proteins that were absent from IgG group, 20 of which are known components of SGs, including G3BP1. Gene Ontology (GO) analysis revealed that the identified proteins were primarily involved in SG assembly, translation, ribosomal biogenesis, and the positive regulation of the apoptotic process (Fig. 3h). Among the proteins associated with apoptosis, receptor for activated C kinase 1 (RACK1) stood out as an activator of the stress-responsive MAPK pathway, and previous studies have demonstrated that SG formation inhibits apoptosis by suppressing RACK1<sup>23</sup>. Supporting this finding, CoIP and IF experiments confirmed that, in response to oxaliplatin, G3BP1 and RACK1, but not TIA1, co-immunoprecipitated with UBAP2L and was recruited to SGs, (Fig. 3i–k). Together, these results suggest that UBAP2L cooperates with G3BP1 to promote SG formation. UBAP2L-nucleated SGs may inhibit the apoptotic pathway by sequestering RACK1 and interfering with its pro-apoptotic function.

### Oxaliplatin triggers phosphorylation and activation of HSF1, enhancing UBAP2L transcription

The mechanism underlying UBAP2L upregulation and SG formation in response to oxaliplatin stress is unknown. Screening transcription factors for potential binding sites on the *UBAP2L* gene promoter using PROMO database identified heat shock factor protein 1 (HSF1), a transcription factor that regulates gene expression under cellular stress, particularly HS. In addition to its role in regulating HS proteins, HSF1 is known to affect a distinct set of genes in cancer cells<sup>24</sup>. To assess whether HSF1 regulates UBAP2L expression, we analyzed UBAP2L levels in different GC cells with varying HSF1 expression. *HSF1* depletion significantly decreased both mRNA and protein levels of UBAP2L while *HSF1* overexpression enhanced UBAP2L expression (Fig. 4a and Supplementary Fig. 6a). HSF1 inhibitor DTHIB also reduced UBAP2L levels (Fig. 4b and Supplementary Fig. 6b). Given the role of HSF1 in the HS response, we investigated whether UBAP2L is regulated under HS conditions. Exposure to HS (42 °C, 0.5 h) induced the mRNA expression of *HSPB1*, a classical HS response gene, but did not affect UBAP2L levels (Supplementary Fig. 6c), indicating that HSF1 regulation of UBAP2L is independent of heat shock. We identified three potential HSF1 binding motifs within the *UBAP2L* promoter region at positions –1882 to –1875, –1287 to –1280, and –62 to –55 (Supplementary Fig. 6d). Chromatin immunoprecipitation (ChIP) assays demonstrated a marked increase in the binding of HSF1 to these specific sites (Supplementary Fig. 6e). Additionally, the luciferase reporter assay showed a significant upregulation of UBAP2L luciferase activity after HSF1 overexpression. Notably, the enhanced transcriptional activation of UBAP2L was disrupted when the binding region was mutated and fully abolished when all three regions were mutated (Fig. 4c, d).

Interestingly, while UBAP2L expression was upregulated in TDOXR cells, total HSF1 levels remained unchanged (Fig. 4e). For HSF1 to take effect

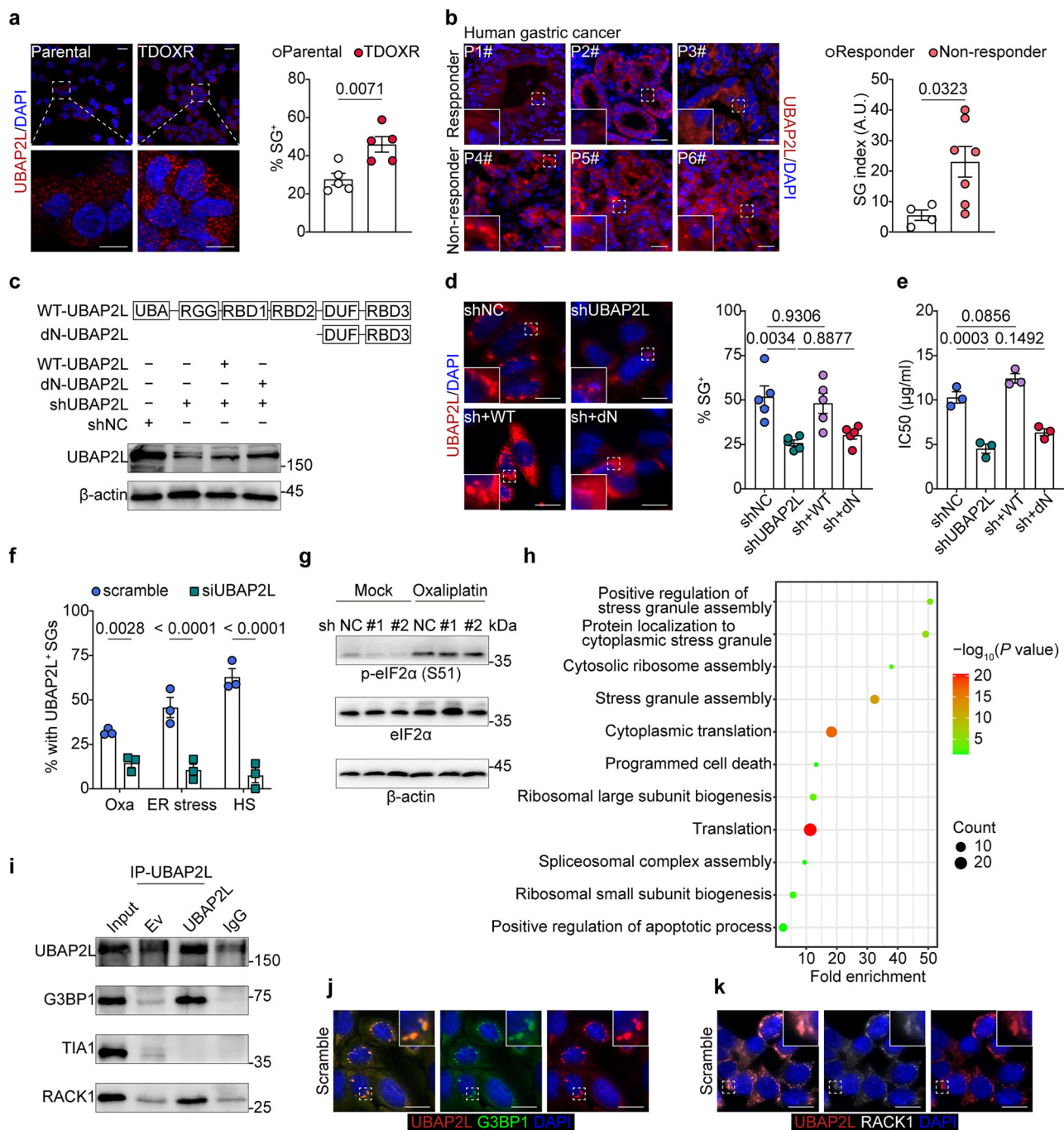
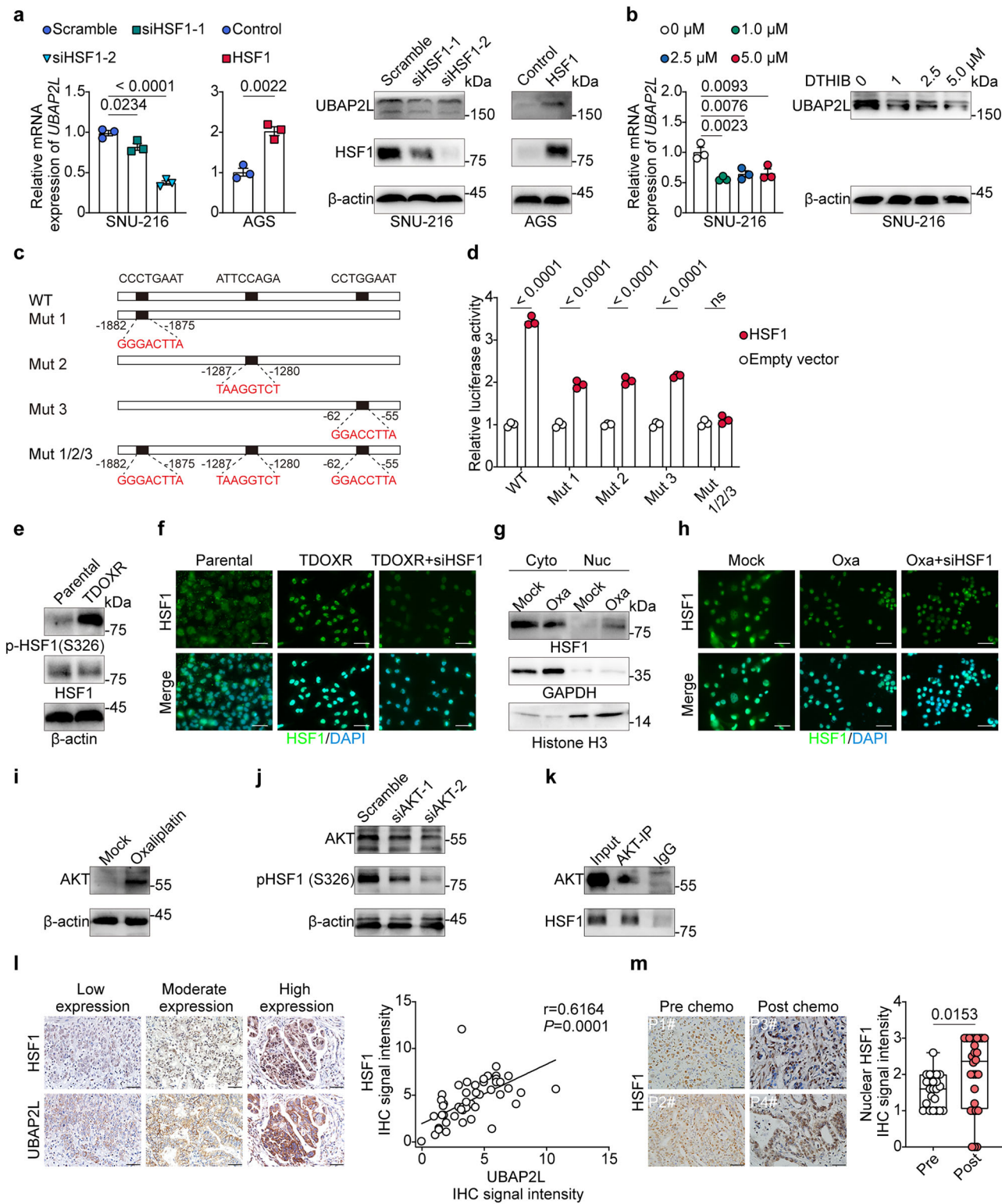


**Fig. 3 | UBAP2L-mediated oxaliplatin resistance is SG dependent.**

**a** Representative IF staining (left) of SGs detected by UBAP2L and quantification (right) of UBAP2L<sup>+</sup> SG-positive parental and TDOXR cells treated with oxaliplatin (10 μg/ml for 8 h) or vehicle control ( $n = 5$  fields per group). Dashed line areas are shown with magnification. Scale bars, 20 μm (overview) and 10 μm (magnified). **b** Representative UBAP2L IF staining (left) and quantification (right) of the SG index in tumor biopsies from responsive ( $n = 4$ ) and non-responsive ( $n = 7$ ) GC patients treated with preoperative oxaliplatin-based chemotherapy. **c** Schematic of UBAP2L expression constructs and WB of lysates of MGC-803 cells expressing the indicated shRNA and shRNA-resistant UBAP2L constructs. **d** Representative IF staining (left) of UBAP2L and quantification (right) of the SG index in MGC-803 cells expressing the indicated constructs as in (c). **e** IC50 assay for oxaliplatin in MGC-803 cells expressing the indicated constructs as in (c). **f** Quantification of SG-positive SGC-7901 cells as detected by G3BP1 with or without UBAP2L knockdown following oxaliplatin (15 μg/ml, 12 h), endoplasmic reticulum (ER) stress (2 mM

DTT, 30 min) or heat shock (HS; 42 °C, 60 min) treatment ( $n = 3$  fields per group). **g** UBAP2L expression does not alter eIF2α phosphorylation levels. WB analysis of WCEs from SGC-7901 cells modified to express negative control short hairpin RNA (shNC) or two independent shRNAs for UBAP2L (#1, #2), treated with oxaliplatin (15 μg/ml, 24 h) or vehicle control. **h** Gene Ontology analysis of SG components enriched from oxaliplatin-treated GC cells. **i** HEK293T cells were transfected with empty vector or UBAP2L plasmid. After 48 h, the cells were lysed and immunoprecipitated with anti-UBAP2L antibody or IgG antibody. The immunoprecipitants were immunoblotted for UBAP2L, G3BP1, TIA1 or RACK1. **j** Representative IF staining of UBAP2L and G3BP1 in MGC-803 cells. **k** Representative IF staining of UBAP2L and RACK1 in MGC-803 cells. Scale bars, 20 μm. Dashed line areas are shown with magnification. *P* values determined by one-way ANOVA with Bonferroni's post hoc test (d, e) or two-tailed unpaired *t*-test (a, b, f). Data are represented as the mean ± s.e.m (a, b, d–f). Data are pooled biological replicates (b) or representative of three independent experiments (a, c–g, i–k).



as a transcription factor, it must be phosphorylated in the cytoplasm before translocating to the nucleus to regulate target genes<sup>35</sup>. We thus postulated that HSF1 undergoes phosphorylation following oxaliplatin treatment. Indeed, we observed increased phosphorylation of HSF1 at serine residue 326 and enhanced nuclear localization of HSF1 in TDOXR cells compared to parental cells (Fig. 4e, f). Additionally, increased nuclear HSF1 levels and enhanced nuclear translocation of HSF1 were also observed in GC cells after oxaliplatin treatment, which was reversible upon *HSF1* silencing (Fig. 4g, h).

Recent studies have highlighted the PI3K/AKT signaling pathway as a key regulator of HSF1 activation at S326 in various cellular contexts, including cancer<sup>26</sup>. Oxaliplatin has been shown to activate the PI3K/AKT pathway<sup>27</sup>. Based on this, we hypothesize that oxaliplatin-induced activation of PI3K/AKT may mediate the phosphorylation of HSF1 at S326. We confirmed that AKT are upregulated following oxaliplatin treatment (Fig. 4i). Moreover, knockdown of AKT significantly reduced the phosphorylation of HSF1 at S326 (Fig. 4j). Immunoprecipitation followed by

**Fig. 4 | Oxaliplatin triggers phosphorylation and activation of HSF1, enhancing UBAP2L transcription.** **a** Quantification of mRNA by RT-PCR (left) and WB analysis (right) for the indicated genes in specified cell lines expressing the indicated constructs. **b** Quantification of mRNA by RT-PCR (left) and WB analysis (right) for the indicated genes in SNU-216 cells treated with HSF inhibitor DTHIB (0, 1.0, 2.5, and 5.0  $\mu$ M). **c** The position of the putative HSF1 binding regions in the human UBAP2L promoter and the schematic diagram of mutated UBAP2L promoter reporter. **d** Relative luciferase activity in 293 T cells co-transfected with empty vector or HSF1 plasmids and indicate wildtype (WT) or mutated UBAP2L promoter reporter. **e** WB analysis of WCEs from parental and TDOXR cells using the indicated antibodies. **f** Representative IF staining of HSF1 in parental cells, TDOXR cells, and TDOXR cells with *HSF1* knockdown. **g** WB analysis of cytoplasmic and nuclear lysates from AGS cells treated with either oxaliplatin (10  $\mu$ g/ml, 24 h) or vehicle control. GAPDH and histone H3 serve as loading controls for cytoplasmic and nuclear lysates, respectively. **h** Representative IF staining of HSF1 in AGS cells following the indicated treatments. **i** WB analysis for the indicated genes in MGC80-

3 cells following oxaliplatin treatment. **j** WB analysis for the indicated genes in MGC80-3 cells with or without *AKT* knockdown. **k** HEK293T cells were lysed and immunoprecipitated with anti-AKT antibody or IgG antibody. The immunoprecipitates were immunoblotted for AKT and HSF1. **l** Representative IHC staining of HSF1 and UBAP2L (left) in 58 GC patient samples, displaying increasing staining intensity. The right panel shows a positive correlation between HSF1 and UBAP2L IHC signal intensities. **m** Representative IHC staining of HSF1 (left) and quantification (right) of nuclear HSF1 signal intensity in 23 pre-chemotherapy and 28 post-chemotherapy GC patient samples. Boxes indicate the 25th to 75th percentiles, whiskers represent the minimum to maximum values, and the center line denotes the median. Scale bar, 50  $\mu$ m. *P* values determined by one-way ANOVA with Bonferroni's post hoc test (**a**, **b**), two-tailed unpaired *t*-test (**a**, **d**, **m**) or Pearson correlation test (**l**). Data are represented as the mean  $\pm$  s.e.m. (**a**, **b**, **d**, **m**). Data are pooled biological replicates (**l**, **m**) or representative of three independent experiments (**a**, **b**, **d**–**k**).

western blotting revealed a constitutive interaction between AKT and HSF1 (Fig. 4k). These findings collectively support our hypothesis that AKT interacts with HSF1 and mediates its phosphorylation at S326.

To assess clinical relevance, we performed IHC staining of HSF1 and UBAP2L in 59 tumor samples from GC patients, suggesting significant coexpression (Fig. 4l). Analysis of TCGA (STAD) and GEO databases corroborated these findings (Supplementary Fig. 6f). Nuclear localization of HSF1 was validated in GC samples following oxaliplatin treatment, with increased staining intensity observed in residual tumor tissues compared to pre-treatment samples (Fig. 4m). These results strongly indicate that oxaliplatin activates HSF1, leading to the transcriptional upregulation of UBAP2L.

### HSF1 induces oxaliplatin resistance via UBAP2L-driven SG formation

We evaluated oxaliplatin sensitivity following *HSF1* knockdown in vitro (Supplementary Fig. 7a). Knockdown of *HSF1* enhanced oxaliplatin sensitivity, resulting in significantly decreased IC50 values and increased apoptosis rates in different GC cells (Supplementary Fig. 7b,c and Supplementary Fig. 8a). These findings were further validated by colony formation assays (Supplementary Fig. 7d). We then examined the role of UBAP2L-mediated SG formation in the inductive effect of HSF1 on oxaliplatin resistance. Restoring UBAP2L expression after *HSF1* knockdown (Fig. 5a) reestablished UBAP2L<sup>+</sup>SG and G3BP1<sup>+</sup>SG formation, while ISRIB treatment diminished this effect (Fig. 5b and Supplementary Fig. 7e). Consistently, increased UBAP2L expression enhanced oxaliplatin resistance, while ISRIB partially reversed this effect (Fig. 5c and Supplementary Fig. 8b). Moreover, *HSF1* overexpression increased resistance, which was mitigated by UBAP2L deletion or ISRIB treatment (Fig. 5d and Supplementary Fig. 8c). Thus, UBAP2L-induced SG formation mediate the role of HSF1 in promoting oxaliplatin resistance.

Clinically, HSF1 levels were found to be elevated in human GC samples compared to paired normal tissues (Supplementary Fig. 7f). The HSF1 high-expression group was significantly associated with a higher proportion of CIN, MSI or POLE subgroups (Supplementary Fig. 7g, Supplementary Table 3). In GC patients, high HSF1 expression correlated with poor clinical responses to preoperative oxaliplatin-based chemotherapy (Fig. 5e). Importantly, the HSF1 expression was positively associated with the level of UBAP2L<sup>+</sup>SGs (Fig. 5f). Analysis indicated that *HSF1* expression was negatively associated with overall survival and progression-free survival in chemotherapy-treated GC patients (Fig. 5g), but not in those undergoing surgery alone (Supplementary Fig. 7h).

### Synergistic effects of ISRIB or DTHIB in targeting oxaliplatin resistance

Our data indicate that SG upregulation in oxaliplatin-resistant cells and tumor samples is driven by transcriptional upregulation of UBAP2L by HSF1, suggesting inhibition of HSF1 or SG formation could overcome this

resistance. To evaluate this idea, we treated nude mice bearing oxaliplatin-sensitive (parental) or resistant (TDOXR) xenograft tumors using SG inhibitor ISRIB, HSF1 inhibitor DTHIB, or their combinations (Fig. 6a). Treatment with oxaliplatin, ISRIB, or DTHIB alone inhibited tumor growth in vivo; however, the combination of oxaliplatin with ISRIB or DTHIB resulted in a significant synergistic effect on tumor growth inhibition (Fig. 6b and Supplementary Fig. 9a). Importantly, ISRIB and DTHIB did not affect animal body weight (Supplementary Fig. 9b). Reduced levels of UBAP2L<sup>+</sup>SG and G3BP1<sup>+</sup>SG, alongside increased CC3-positive or TUNEL-positive area were observed from xenografts in the combination treatment group (Fig. 6d and Supplementary Fig. 9e). Furthermore, DTHIB effectively targeted TDOXR xenograft tumors, which remained highly sensitive to both DTHIB alone and the combination with oxaliplatin (Fig. 6c and Supplementary Fig. 9c). No significant weight loss was observed in DTHIB-treated mice (Supplementary Fig. 9d). The combination treatment group showed decreased levels of UBAP2L<sup>+</sup>SG and G3BP1<sup>+</sup>SG, as well as elevated CC3-positive and TUNEL-positive area (Fig. 6e and Supplementary Fig. 9f).

To fully capture the complexity of the tumor microenvironment, we established a genetically modified spontaneous GC mice model. This model is generated by crossing the gastric epithelium-specific Cre strain *Claudin18-Cre<sup>ERT2</sup>* with mice carrying conditional alleles for *Kras<sup>LSL-G12D/+</sup>*, *Trp53<sup>loxP/loxP</sup>*, and *Apc<sup>loxP/loxP</sup>* (Fig. 6f)<sup>28</sup>, and was subjected to tamoxifen induction and subsequent oxaliplatin treatment (Fig. 6g). Our results indicate that the levels of UBAP2L<sup>+</sup>SG were significantly higher, while the areas positive for CC3 and TUNEL were significantly lower in the non-responsive GC mouse group compared to the responsive group (Fig. 6h). Together, these findings suggest that inhibiting HSF1 or SG may effectively overcome both intrinsic and acquired resistance to oxaliplatin.

### Discussion

In this study, we demonstrate that oxaliplatin uniquely induces translational arrest and SG formation, in contrast to other platinum-based drugs. Here, we establish a causal link between SG formation and oxaliplatin resistance. GC resist oxaliplatin through enhanced formation of UBAP2L-nucleated SGs, which sequester RACK1, a pro-apoptotic factor, thereby inhibiting apoptotic pathway. UBAP2L upregulation is triggered by oxaliplatin-induced phosphorylation of HSF1 via AKT. Inhibition of SG formation or HSF1 activity impairs oxaliplatin resistance, highlighting potential therapeutic strategy to overcome oxaliplatin resistance (Fig. 7).

This study highlights UBAP2L as the key SG nucleator in response to oxaliplatin. Our findings do not contradict the established role of G3BP1 as a key SG nucleator. G3BP1-positive SGs were infrequently observed in UBAP2L-depleted cells, suggesting that while G3BP1 is not essential for the initial formation of UBAP2L-positive SGs, it may play a critical role in recruiting other components and facilitating SG maturation. Consistent with this, we observed a reduction in UBAP2L granule size following G3BP1 depletion (Supplementary Fig. 5g). We hypothesize that in the absence of

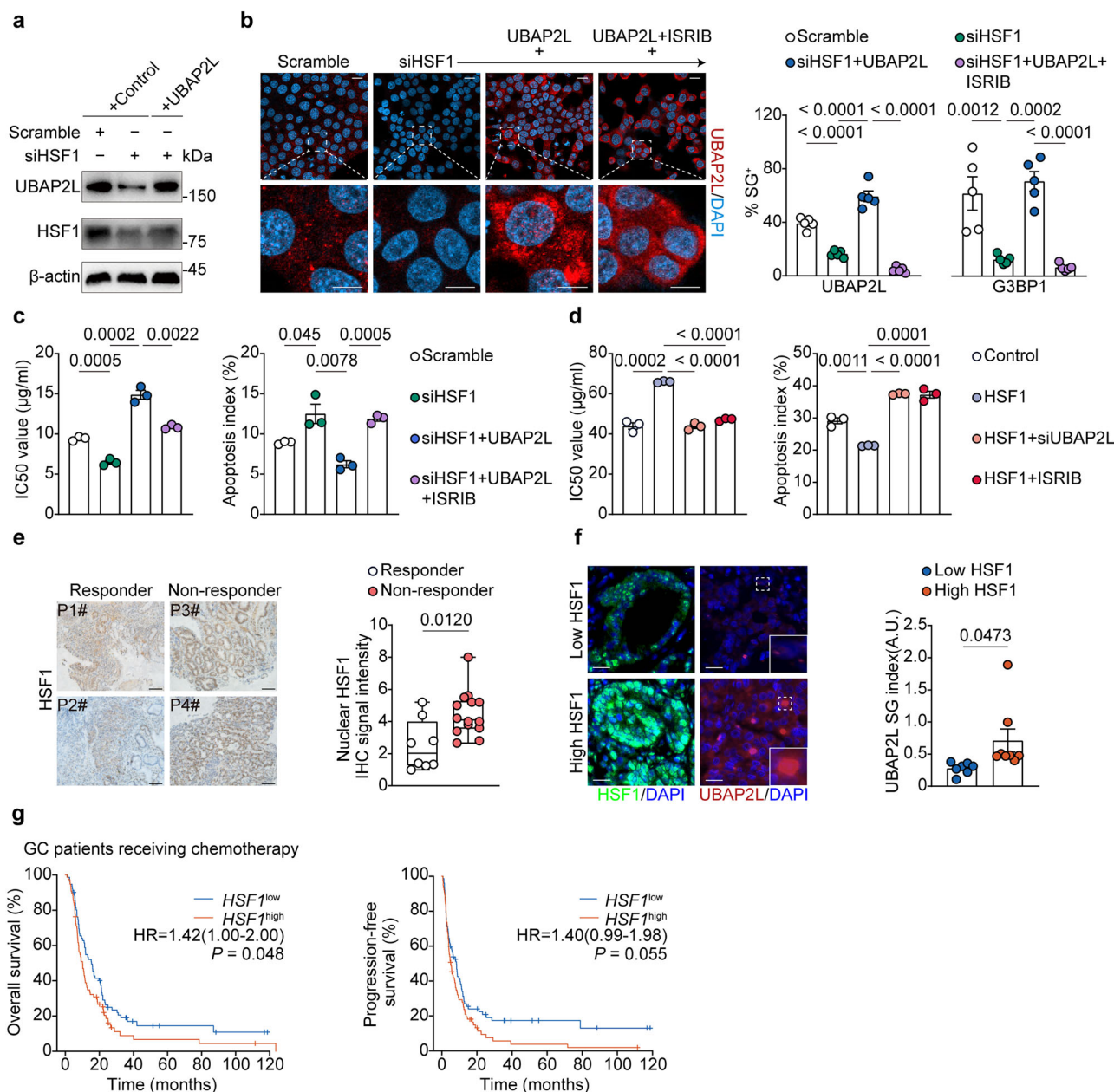


**Fig. 5 | HSF1 induces oxaliplatin resistance via UBAP2L-driven SG formation.** **a** WB analysis of WCEs from *HSF1*-depleted SGC-7901 cells complemented with either *UBAP2L* or control plasmid, using the indicated antibodies. **b** Representative IF staining of UBAP2L (left) and quantification (right) of SG-positive SGC-7901 cells expressing the constructs from **a**, with or without ISIRIB (5  $\mu$ M, 12 h). The dashed line indicates the magnified area. Scale bars, 20  $\mu$ m (overview) and 10  $\mu$ m (magnified). **c** IC<sub>50</sub> assay for oxaliplatin and FCM analysis of apoptosis rates in MGC80-3 cells expressing the constructs from **a**, with or without ISIRIB (5  $\mu$ M, 24 h). **d** IC<sub>50</sub> assay for oxaliplatin and FCM analysis of apoptosis rates in *HSF1*-over-expressed AGS cells complemented with siRNA targeting *UBAP2L* or control siRNA, with or without ISIRIB (5  $\mu$ M, 24 h). **e** Representative IHC staining of HSF1 (left) and quantification (right) of IHC signal intensity in tumor biopsies from

responsive ( $n = 8$ ) and non-responsive ( $n = 14$ ) GC patients treated with pre-operative oxaliplatin-based chemotherapy. Scale bars, 50  $\mu$ m. Boxes represent the 25th to 75th percentiles, whiskers indicate minimum to maximum values, and the center line denotes the median. **f** Representative IF staining of HSF1 and UBAP2L (left) and quantification (right) of SG index as detected by UBAP2L from human GC tumor samples. Scale bars, 20  $\mu$ m. **g** Negative correlation between *HSF1* expression and overall survival or progression-free survival in GC patients treated with chemotherapy, based on data from the Kaplan-Meier Plotter database. *P* values determined by one-way ANOVA with Bonferroni's post hoc test (**b–d**), two-tailed unpaired *t*-test (**e, f**) or log-rank test (**g**). Data are represented as the mean  $\pm$  s.e.m (**b–d, f**). Data are pooled biological replicates (**e, f**) or representative of three independent experiments (**a–d**).

G3BP1, only isolated UBAP2L cores assemble, implying that, under normal conditions, UBAP2L cores form first. G3BP1 core formation is likely subsequently facilitated by UBAP2L and is crucial for SG maturation. Additionally, the interplay between UBAP2L and other nucleators may involve complex regulatory networks that have yet to be fully explored. These interactions could potentially influence SG dynamics and their role in stress resistance, warranting further investigation.

SG composition may vary depending on the type of stress and cellular environment, implying that the same set of SG nucleators may contribute variably to stress adaptation under different conditions. For instance, certain SG components, like YWHAZ and TM4SF1-AS1<sup>29,30</sup>, that are prominent in GC cells may be less abundant or absent in other cell types, reflecting the unique molecular pathways and stress adaptations associated with cancer biology. This heterogeneity in SG composition underscores the complexity

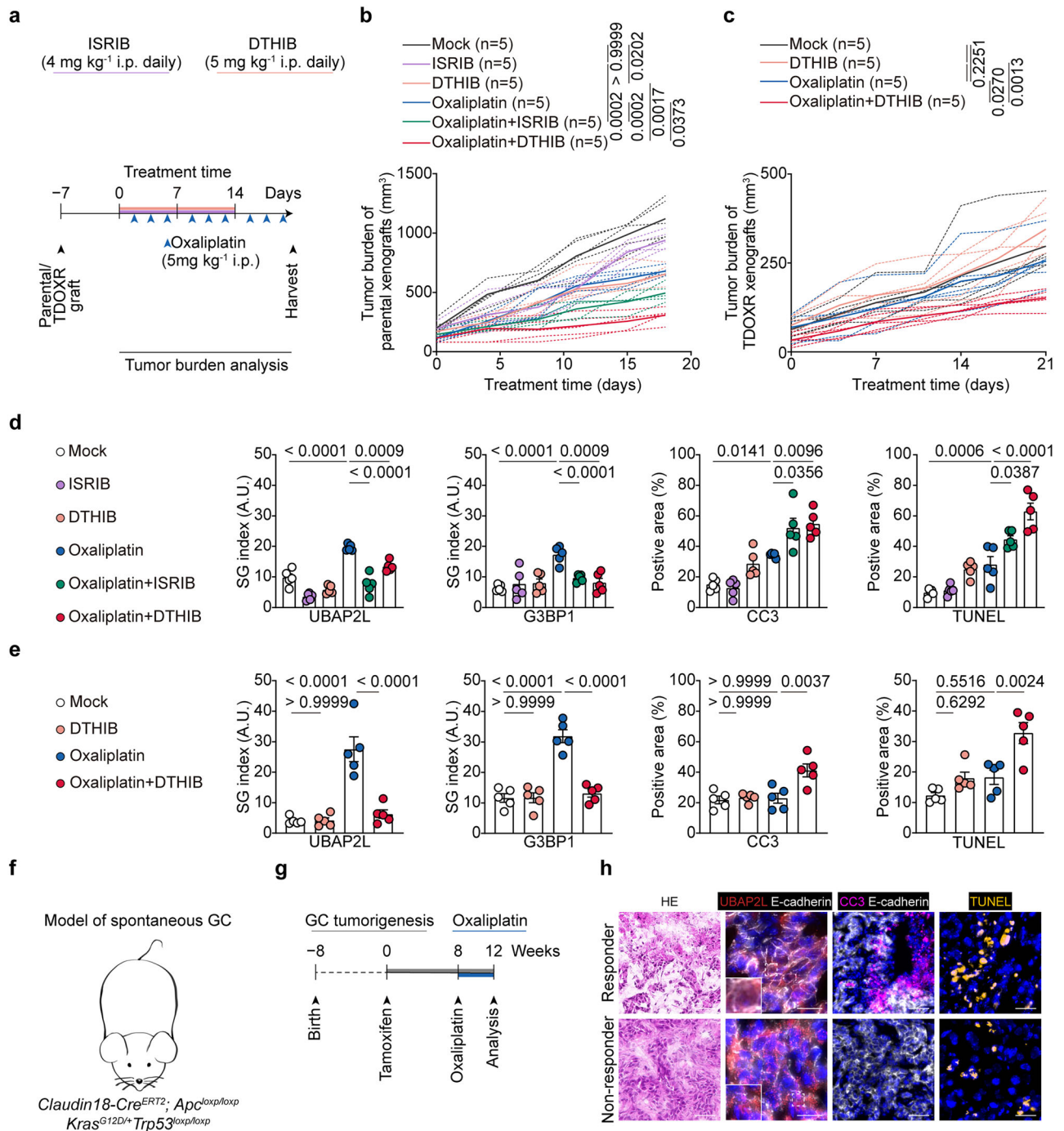
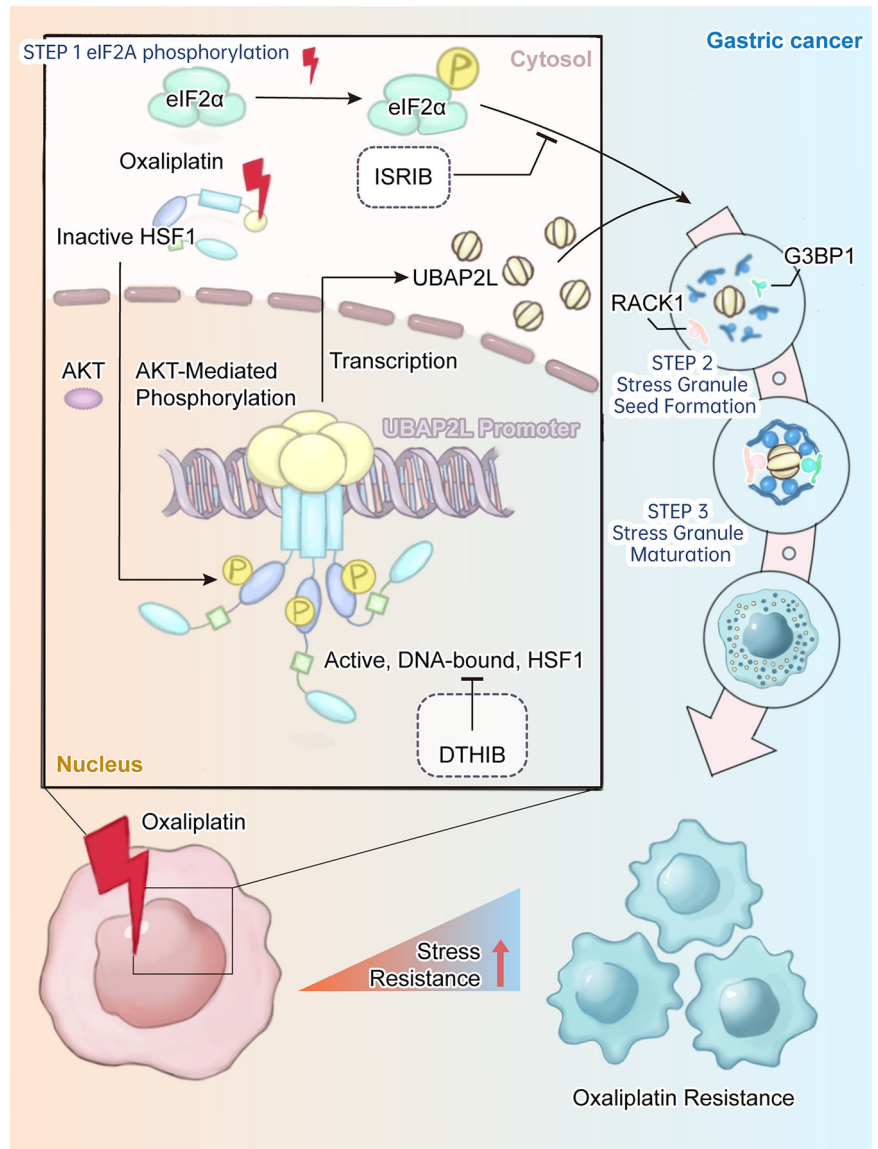


**Fig. 6 | Synergistic effects of ISRIB or DTHIB in targeting oxaliplatin resistance.** **a** Experimental design for assessing combination therapies in oxaliplatin-sensitive (parental) and oxaliplatin-resistant (TDOXR) mouse models. **b** Quantification of tumor burden in parental xenografts of nude mice treated with vehicle control, oxaliplatin (5 mg/kg, three times per week), alone or in combination with ISRIB (4 mg/kg, once daily for two consecutive weeks) or DTHIB (5 mg/kg, once daily for two consecutive weeks) (*n* = 5 mice per group). **c** Tumor burden quantification in TDOXR xenografts of nude mice treated with vehicle control, oxaliplatin (5 mg/kg, three times per week), alone or in combination with DTHIB (5 mg/kg, once daily for two consecutive weeks) (*n* = 5 mice per group). **d** Quantification of the SG index as detected by UBAP2L or G3BP1, and CC3-positive area or TUNEL-positive area from xenograft tumors in (b). **e** Quantification of the SG index as detected by

UBAP2L or G3BP1, and CC3-positive area or TUNEL-positive area from xenograft tumors in c. **f** Schematic of generation of spontaneous GC mouse model. Tamoxifen-induced recombination of mutant alleles is mediated using a gastric-specific *Claudin18-Cre<sup>ERT2</sup>* strain. **g** Experimental design for tamoxifen-induced recombination and oxaliplatin treatment in spontaneous GC mouse model. **h** Representative HE staining, and IF staining of UBAP2L, E-cadherin, CC3, and TUNEL in spontaneous GC tumors according to their response to oxaliplatin treatment. The dashed line indicates the magnified area. Scale bars, 50 μm (UBAP2L/E-cadherin), otherwise 20 μm. *P* values determined by two-way ANOVA with Bonferroni's post hoc test (b, c) or one-way ANOVA with Bonferroni's post hoc test (d, e). Data are represented as the mean ± s.e.m (d, e). Data are pooled biological replicates (b, c, h).

**Fig. 7 | SGs are phase-separating organelles that act as protective mechanisms in response to various harmful stimuli, but their role in oxaliplatin resistance remains unclear. GC resist oxaliplatin through forming UBAP2L-nucleated SG which sequester RACK1, preventing the initiation of apoptotic pathway. Transcriptional upregulation of UBAP2L is enhanced by oxaliplatin-induced phosphorylation of heat shock factor protein 1 (HSF1) via AKT. Under oxaliplatin stress, the SG seed nucleated by UBAP2L recruits other SG proteins like G3BP1 and RACK1 and matures over time, ultimately enhancing resistance to oxaliplatin.**



of SG function and highlights the need for further research to elucidate how these differences influence cellular stress responses and disease progression. Future studies comparing SG dynamics across diverse cell types and stress conditions could provide valuable insights into the context-specific roles of SGs in health and disease.

Previous study suggested that oxaliplatin induces ribosome biogenesis stress (RBS), leading to a distinct translational arrest mechanism compared to cisplatin and carboplatin<sup>1</sup>. RBS refers to a cellular state where the normal protein synthesis machinery is disrupted or impaired, causing a slowdown or complete halt in translation<sup>31</sup>. This translational arrest is a key trigger for the formation of SGs, which are cytoplasmic aggregates that form when translationally stalled mRNAs and their associated proteins accumulate. In the current study, oxaliplatin induced phosphorylation and activation of HSF1, which raises the question regarding the role of RBS in HSF1 activation. Previous studies found that HSF1 serves as a critical response factor in RBS, at least in *Saccharomyces cerevisiae*, where it helps reinforce the proteostasis network to mitigate RBS<sup>32,33</sup>. When ribosomal RNA processing or ribosomal protein assembly is inhibited, cells adapt a rapid activation of HSF1, and correspondingly upregulates chaperon proteins that facilitates protein folding, degradation machinery that clears away abnormal or excessive proteins, and other HSF1 target genes that collectively restore proteostasis. More importantly, this response is highly specific<sup>33</sup>. HSF1

activation occurs without activating a general environmental stress response (ESR) driven by Msn 2/4, suggesting a distinct regulatory mechanism for RBS adaption<sup>33</sup>. Although these findings primarily derive from yeast model, the conservation of HSF1, chaperones, and the proteostasis network across eukaryotes implies that a similar RBS response may exist in human cells, particularly in highly proliferative cells like cancer cells that rely on rapid ribosome biogenesis. Therefore, it is plausible to suggest that oxaliplatin induces RBS, leading to the phosphorylation and activation of HSF1. Future study should pay more attention on whether and how HSF1 is employed in the oxaliplatin-induced RBS adaption in cancers, and targeting strategy that overcomes oxaliplatin resistance.

From a therapeutic perspective, targeting HSF1 or SGs, key mediators of oxaliplatin resistance, offers potential for improving treatment outcomes. Our data suggest that combining oxaliplatin with SG inhibitors (such as ISRIB) or HSF1 inhibitors (such as DTHIB) significantly enhances its efficacy. What cannot be ignored is that ISRIB and DTHIB monotherapy also exhibited anticancer activity themselves. This is reasonable because HSF1 and SGs assembly were both reported to be associated with not only chemotherapy resistance but also tumorigenesis and cancer progression<sup>34,35</sup>. However, since they are strongly induced under stress conditions, applying SGs or HSF1 inhibitors in combination with conventional chemotherapy is expected to disrupt the protective mechanisms that cancer cells rely on

during cytotoxic stress. This approach would likely make the best use of their inhibition, and significantly enhance the anticancer effects of these agents while minimizing additional harm to normal cells. This synergistic strategy forms the central focus of the translational approaches, aiming to develop more effective therapeutic regimens for GC.

The clinical application of ISRIB and HSF1 inhibitors also raise several potential considerations. While these inhibitors show promise in preclinical models, their clinical applicability, toxicity profiles, and effectiveness in combination therapies require thorough evaluation in clinical trials. SGs play a crucial role in cellular stress responses, metabolic homeostasis, and mammalian development<sup>35–40</sup>. Disrupting SGs with ISRIB could interfere with their physiological functions, potentially impairing cellular self-protection mechanisms in response to stressors such as infections or injuries, leading to tissue damage. SGs are also involved in activating endogenous immunity and inhibiting apoptosis under stress, making their disruption particularly concerning. While ISRIB demonstrates good *in vivo* stability and brain permeability<sup>41–43</sup>, limited information about its metabolic pathways, excretion mechanisms, tumor distribution, and pharmacokinetics in humans significantly restricts its clinical translation. Moreover, ISRIB has a narrow therapeutic window, being effective at suppressing low levels of integrated stress response (ISR) activity but ineffective against strong ISR activation<sup>43</sup>, which may limit its application in cancer therapy. The HSF1 inhibitor DTHIB also exhibits cytotoxic effects on normal liver and kidney cells, particularly at higher doses<sup>44–46</sup>. Although DTHIB shows tumor-targeting properties and is widely distributed in the body<sup>47</sup>, its poor water solubility results in low oral bioavailability, necessitating further development of drug delivery systems to enhance its bioavailability<sup>46</sup>.

Despite the valuable insights gained in this study, several limitations must be acknowledged. The localization of UBAP2L to SGs in response to oxaliplatin or other stressors demonstrates that SG composition is context-dependent. Previous research has indicated that SG composition can change under different stress conditions. GC patients typically undergo treatments involving combinations of chemotherapy, targeted therapies, and immunotherapies, which may modify the composition of SG components and their associated nucleators. However, the interactions between these treatments and SG dynamics are complex and not yet fully understood. Thus, it is essential to carefully consider the role of UBAP2L and other SG nucleators in the context of combination therapies.

The mechanisms by which UBAP2L mediates SG formation remain to be fully characterized. The key nodes of the core SG network are known to contribute to SG formation to varying extents, and it is possible that UBAP2L, stimulated by oxaliplatin, may influence their contribution. This aligns with the predicted model, where SG assembly is regulated by the positive and negative cooperativity of extrinsic factors interacting with the core network<sup>9</sup>. In support of this, we propose that UBAP2L may cooperate with G3BP1 to facilitate SG formation. As a core component of the SG network, G3BP1 may serve as a mechanism through which UBAP2L alters the core interaction network to promote SG assembly. This suggests that other proteins may also be involved in SG nucleation and maturation in response to oxaliplatin or other stressors. Additionally, it is possible that UBAP2L, as a constituent of SGs, may itself contribute to the core SG network in cells treated with oxaliplatin. Clearly, to better understand this process, further research is needed to map the entire SG interaction network.

Finally, while our study suggests that the expression of UBAP2L and the presence of UBAP2L-nucleated SGs could serve as biomarkers for predicting treatment response, large-scale clinical validation is required. It is important to emphasize that these results are based on preliminary evidence, and further validation in larger, independent patient cohorts with well-defined clinical characteristics and treatment histories is required before UBAP2L can be considered for clinical use. The current study is also limited by the sample size and heterogeneity of the clinical cohort, which may affect the generalizability of the findings. Future studies could focus on validating UBAP2L as a biomarker in prospective, multicenter trials to confirm its clinical utility. Furthermore, the variability in SG composition

and nucleator activity across different patients and tumor types complicates the use of these biomarkers in clinical practice. Future studies should aim to refine these biomarkers and explore how they can be integrated into personalized treatment strategies.

## Conclusion

In summary, we demonstrate that GC resist oxaliplatin through enhanced formation of UBAP2L-nucleated SGs, which sequester RACK1, a pro-apoptotic factor, thereby inhibiting apoptotic pathway. The transcriptional upregulation of UBAP2L is driven by the phosphorylation and activation of HSF1 via AKT. Our results offer new insights into the role of UBAP2L-nucleated SGs in mediating oxaliplatin resistance. Consequently, targeting SG formation or HSF1 presents a promising therapeutic approach to address oxaliplatin resistance.

## Data availability

Plasmids, antibodies and cell lines generated in this study will be available from the corresponding author upon request with a completed material transfer agreement. MS data have been deposited into the ProteomeXchange Consortium through the PRIDE partner repository with the dataset identifiers PXD065770. The source data behind the graphs in the paper can be found in Supplementary Data 1.

Received: 14 January 2025; Accepted: 24 July 2025;

Published online: 13 August 2025

## References

- Bruno, P. M. et al. A subset of platinum-containing chemotherapeutic agents kills cells by inducing ribosome biogenesis stress. *Nat. Med.* **23**, 461–471 (2017).
- Glauninger, H., Wong Hickernell, C. J., Bard, J. A. M. & Drummond, D. A. Stressful steps: Progress and challenges in understanding stress-induced mRNA condensation and accumulation in stress granules. *Mol. Cell* **82**, 2544–2556 (2022).
- Millar, S. R. et al. A new phase of networking: the molecular composition and regulatory dynamics of mammalian stress granules. *Chem. Rev.* **123**, 9036–9064 (2023).
- Fujikawa, D. et al. Stress granule formation inhibits stress-induced apoptosis by selectively sequestering executioner caspases. *Curr. Biol.* **33**, 1967–1981.e1968 (2023).
- Zhao, Z. et al. QKI shuttles internal m(7)G-modified transcripts into stress granules and modulates mRNA metabolism. *Cell* **186**, 3208–3226.e3227 (2023).
- Sanders, D. W. et al. Competing Protein-RNA interaction networks control multiphase intracellular organization. *Cell* **181**, 306–324.e328 (2020).
- Mehta, S. & Zhang, J. Liquid-liquid phase separation drives cellular function and dysfunction in cancer. *Nat. Rev. Cancer* **22**, 239–252 (2022).
- Alberti, S., Gladfelter, A. & Mittag, T. Considerations and challenges in studying liquid-liquid phase separation and biomolecular condensates. *Cell* **176**, 419–434 (2019).
- Yang, P. et al. G3BP1 is a tunable switch that triggers phase separation to assemble stress granules. *Cell* **181**, 325–345.e328 (2020).
- Lin, C. et al. Modulation of YBX1-mediated PANoptosis inhibition by PPM1B and USP10 confers chemoresistance to oxaliplatin in gastric cancer. *Cancer Lett.* **587**, 216712 (2024).
- Tang, X. et al. Upregulation of CRABP2 by TET1-mediated DNA hydroxymethylation attenuates mitochondrial apoptosis and promotes oxaliplatin resistance in gastric cancer. *Cell Death Dis.* **13**, 848 (2022).
- Cerami, E. et al. The cBio cancer genomics portal: an open platform for exploring multidimensional cancer genomics data. *Cancer Discov.* **2**, 401–404 (2012).

13. Tang, Z. et al. GEPIA: a web server for cancer and normal gene expression profiling and interactive analyses. *Nucleic Acids Res.* **45**, W98–w102 (2017).
14. Györfy, B. Integrated analysis of public datasets for the discovery and validation of survival-associated genes in solid tumors. *Innovations* **5**, 100625 (2024).
15. Zismanov, V. et al. Phosphorylation of eIF2 $\alpha$  is a translational control mechanism regulating muscle stem cell quiescence and self-renewal. *Cell Stem Cell* **18**, 79–90 (2016).
16. McDermott, M. et al. In vitro development of chemotherapy and targeted therapy drug-resistant cancer cell lines: a practical guide with case studies. *Front Oncol.* **4**, 40 (2014).
17. Bezu, L. et al. eIF2 $\alpha$  phosphorylation is pathognomonic for immunogenic cell death. *Cell Death Differ.* **25**, 1375–1393 (2018).
18. Cui, Q. et al. Diverse CMT2 neuropathies are linked to aberrant G3BP interactions in stress granules. *Cell* **186**, 803–820.e825 (2023).
19. Prentzell, M. T. et al. G3BPs tether the TSC complex to lysosomes and suppress mTORC1 signaling. *Cell* **184**, 655–674.e627 (2021).
20. Zyryanova, A. F. et al. ISRIB blunts the integrated stress response by allosterically antagonising the inhibitory effect of phosphorylated eIF2 on eIF2B. *Mol. Cell* **81**, 88–103.e106 (2021).
21. Huang, C. et al. UBAP2L arginine methylation by PRMT1 modulates stress granule assembly. *Cell Death Differ.* **27**, 227–241 (2020).
22. Kaehler, C., Isensee, J., Hucho, T., Lehrach, H. & Krobitsch, S. 5-Fluorouracil affects assembly of stress granules based on RNA incorporation. *Nucleic Acids Res* **42**, 6436–6447 (2014).
23. Arimoto, K., Fukuda, H., Imajoh-Ohmi, S., Saito, H. & Takekawa, M. Formation of stress granules inhibits apoptosis by suppressing stress-responsive MAPK pathways. *Nat. Cell Biol.* **10**, 1324–1332 (2008).
24. Mendillo, M. L. et al. HSF1 drives a transcriptional program distinct from heat shock to support highly malignant human cancers. *Cell* **150**, 549–562 (2012).
25. Sakurai, H. & Enoki, Y. Novel aspects of heat shock factors: DNA recognition, chromatin modulation and gene expression. *Febs j.* **277**, 4140–4149 (2010).
26. Carpenter, R. L., Paw, I., Dewhirst, M. W. & Lo, H. W. Akt phosphorylates and activates HSF-1 independent of heat shock, leading to Slug overexpression and epithelial-mesenchymal transition (EMT) of HER2-overexpressing breast cancer cells. *Oncogene* **34**, 546–557 (2015).
27. Lin, L. et al. ATXN2L upregulated by epidermal growth factor promotes gastric cancer cell invasiveness and oxaliplatin resistance. *Cell Death Dis.* **10**, 173 (2019).
28. Fatehullah, A. et al. A tumour-resident Lgr5(+) stem-cell-like pool drives the establishment and progression of advanced gastric cancers. *Nat. Cell Biol.* **23**, 1299–1313 (2021).
29. Zhao, J. et al. G3BP1 interacts with YWHAZ to regulate chemoresistance and predict adjuvant chemotherapy benefit in gastric cancer. *Br. J. Cancer* **124**, 425–436 (2021).
30. Kitajima, H. et al. TM4SF1-AS1 inhibits apoptosis by promoting stress granule formation in cancer cells. *Cell Death Dis.* **14**, 424 (2023).
31. Bursać, S., Prodan, Y., Pullen, N., Bartek, J. & Volarević, S. Dysregulated Ribosome biogenesis reveals therapeutic liabilities in cancer. *Trends Cancer* **7**, 57–76 (2021).
32. Albert, B. et al. A ribosome assembly stress response regulates transcription to maintain proteome homeostasis. *Elife* **8**, <https://doi.org/10.7554/eLife.45002> (2019).
33. Tye, B. W. et al. Proteotoxicity from aberrant ribosome biogenesis compromises cell fitness. *Elife* **8**, <https://doi.org/10.7554/eLife.43002> (2019).
34. Dai, C. & Sampson, S. B. HSF1: Guardian of proteostasis in cancer. *Trends Cell Biol.* **26**, 17–28 (2016).
35. Redding, A. & Grabocka, E. Stress granules and hormetic adaptation of cancer. *Trends Cancer* **9**, 995–1005 (2023).
36. Amen, T. & Kaganovich, D. Stress granules inhibit fatty acid oxidation by modulating mitochondrial permeability. *Cell Rep.* **35**, 109237 (2021).
37. Jia, X. et al. De novo variants in genes regulating stress granule assembly associate with neurodevelopmental disorders. *Sci. Adv.* **8**, eabo7112 (2022).
38. Costa-Mattioli, M. & Walter, P. The integrated stress response: From mechanism to disease. *Science* **368**, <https://doi.org/10.1126/science.aat5314> (2020).
39. Harding, H. P., Zhang, Y., Bertolotti, A., Zeng, H. & Ron, D. Perk is essential for translational regulation and cell survival during the unfolded protein response. *Mol. Cell* **5**, 897–904 (2000).
40. Scheuner, D. et al. Translational control is required for the unfolded protein response and in vivo glucose homeostasis. *Mol. Cell* **7**, 1165–1176 (2001).
41. Sidrauski, C. et al. Pharmacological brake-release of mRNA translation enhances cognitive memory. *Elife* **2**, e00498 (2013).
42. Halliday, M. et al. Partial restoration of protein synthesis rates by the small molecule ISRIB prevents neurodegeneration without pancreatic toxicity. *Cell Death Dis.* **6**, e1672 (2015).
43. Rabouw, H. H. et al. Small molecule ISRIB suppresses the integrated stress response within a defined window of activation. *Proc. Natl. Acad. Sci. USA* **116**, 2097–2102 (2019).
44. Nie, Y. et al. Dihydrotanshinone I targets ESR1 to induce DNA double-strand breaks and proliferation inhibition in hepatocellular carcinoma. *Phytomedicine* **130**, 155767 (2024).
45. Ge, M. et al. The anti-hepatic fibrosis effects of dihydrotanshinone I are mediated by disrupting the yes-associated protein and transcriptional enhancer factor D2 complex and stimulating autophagy. *Br. J. Pharm.* **174**, 1147–1160 (2017).
46. Niu, X. et al. Hepatic stellate cell- and liver microbiome-specific delivery system for Dihydrotanshinone I to Ameliorate liver fibrosis. *ACS Nano* **17**, 23608–23625 (2023).
47. Yue, J. et al. The multifaceted mechanisms of Dihydrotanshinone I in the treatment of tumors. *Biomed. Pharmacother.* **175**, 116635 (2024).

## Acknowledgements

This work was supported by Guangdong Basic and Applied Basic Research Foundation (2025A1515012535), China Postdoctoral Science Foundation (2023M741579), Research Fund of Nanfang Hospital, Southern Medical University (2023A021), Key Areas Research and Development Programs of Guangdong Province (2023B1111050009), and Key Clinical Technique of Guangzhou (2023P-ZD01). We sincerely thank Prof. Shun Li for generously providing the spontaneous GC mice, Dr. Zepang Sun and Dr. Lingzhi Wang for their insightful feedback during manuscript revision.

## Author contributions

CR.W., Y.Y., and GX.L. conceived and designed the study. CR.W., RY.L., and XT.L. acquired the data and performed the bioinformatics analysis. CR.W., Y.Y., ZY.L., QC.C., YM.P., BY.Z., QB.Y., GT.Y., and JY.H. performed the experiments. CR.W., Y.Y., ZY.L., and QC.C. drafted the manuscript. CR.W., Y.Y., ZY.L., QC.C., WH.M., and GX.L. reviewed and revised the manuscript. All authors have read and approved the final version of the manuscript.

## Competing interests

The authors declare no competing interests.

## Ethics approval and consent to participate

Approval for the collection of human samples was obtained from the Department of General Surgery at Nanfang Hospital, Southern Medical University. All experiments were approved by the Animal Care and Use Committee of Shenzhen Majory Biotechnology Co., Ltd., and institutional Review Board of Nanfang Hospital, Southern Medical University. Written informed consent was obtained from all participants. The procedures were conducted in accordance with the Declaration of Helsinki guidelines.

## Additional information

**Supplementary information** The online version contains supplementary material available at <https://doi.org/10.1038/s42003-025-08584-w>.

**Correspondence** and requests for materials should be addressed to Zhiying Lian or Guoxin Li.

**Peer review information** *Communications Biology* thanks Jin-A Lee, Zefeng Liu and Yosuke Tanaka for their contribution to the peer review of this work. Primary Handling Editor: Johannes Stortz.

**Reprints and permissions information** is available at <http://www.nature.com/reprints>

**Publisher's note** Springer Nature remains neutral with regard to jurisdictional claims in published maps and institutional affiliations.

**Open Access** This article is licensed under a Creative Commons Attribution-NonCommercial-NoDerivatives 4.0 International License, which permits any non-commercial use, sharing, distribution and reproduction in any medium or format, as long as you give appropriate credit to the original author(s) and the source, provide a link to the Creative Commons licence, and indicate if you modified the licensed material. You do not have permission under this licence to share adapted material derived from this article or parts of it. The images or other third party material in this article are included in the article's Creative Commons licence, unless indicated otherwise in a credit line to the material. If material is not included in the article's Creative Commons licence and your intended use is not permitted by statutory regulation or exceeds the permitted use, you will need to obtain permission directly from the copyright holder. To view a copy of this licence, visit <http://creativecommons.org/licenses/by-nc-nd/4.0/>.

© The Author(s) 2025

---

<sup>1</sup>Department of General Surgery & Guangdong Provincial Key Laboratory of Precision Medicine for Gastrointestinal Tumor, Nanfang Hospital, Southern Medical University, Guangzhou, Guangdong, China. <sup>2</sup>Department of Immunology, Shenzhen Majory Biotechnology Co. Ltd., Shenzhen, China. <sup>3</sup>Department of Anesthesiology, The Third Xiangya Hospital, Central South University, Changsha, China. <sup>4</sup>Departments of Colorectal Surgery, State Key Laboratory of Oncology in South China, Guangdong Provincial Clinical Research Center for Cancer, Sun Yat-sen University Cancer Center, Guangzhou, China. <sup>5</sup>Department of Burn and Plastic Surgery, Southern Theater General Hospital, Guangzhou, China. <sup>6</sup>Department of Gastrointestinal Surgery, The First Affiliated Hospital of Guangzhou Medical University, Guangzhou, China. <sup>7</sup>Department of breast surgery, Affiliated Hospital of Guangdong Medical University, Zhanjiang, China. <sup>8</sup>Zhanjiang Key Laboratory of Intelligent Diagnosis and Treatment of Breast Cancer, Zhanjiang, China. <sup>9</sup>Department of Gastrointestinal Surgery, The First Affiliated Hospital of Guangzhou University of Chinese Medicine, Guangdong Clinical Research Academy of Chinese Medicine, Guangzhou, China. <sup>10</sup>Cancer Center of Beijing Tsinghua Changgung Hospital, School of Clinical Medicine, Tsinghua Medicine, Tsinghua University, Beijing, China. <sup>11</sup>These authors contributed equally: Chaorui Wu, Yu Yan, Qichen Chen.

✉ e-mail: [gzlianzzy@163.com](mailto:gzlianzzy@163.com); [gzliguoxin@163.com](mailto:gzliguoxin@163.com)